Abstract

To achieve future climate goals, UN climate regulations require companies to reduce the global carbon footprint. Elkem ASA is researching how today's coal and coke used in the quartz reduction process can be replaced with a sustainable option for future silicon production. This has started a research collaboration with SINTEF where one of the focus areas is the use of biochar as a reduction agent. The method being investigated is thermal conversion of wood chips into charcoal through a pyrolysis process. The aim of this task has been to simulate this process numerically.

The thesis uses computational fluid dynamics (CFD) in which the mass and heat transport have been studied. Study of relevant literature and simplifications has enabled a numerical simulation of pyrolysis. An important part of the task has been to find properties for the wood chips that will be thermally converted to charcoal. These properties have then been integrated into the numerical models whose task has been to define a porous domain. The models have been built up by 4 steps, each of which are CFD models that gradually increase in complexity. The result has been four models that demonstrate each task. The models have shown that good approaches of pyrolysis, in terms of mass and heat flow, can be demonstrated without involving chemical kinetics schemes. Results indicate that the accumulated mass leaving the reactor during the process is about 75% of the original mass. The heating time takes about 100 minutes before an approximately constant temperature can be seen in the biomass. Furthermore, the results show that a pressure drop through the porous domain is negligible. Mass and energy conservation have been carried out on the system. The calculations show that the conservation laws are satisfied for stationary flows, however more work will be needed to improve the conservation laws for transient flows.

Sammendrag

For å nå fremtidige klimamål, pålegger FN bedrifter utslippskrav i økende mengder for å stramme inn globale karbonutslipp. Elkem ASA forsker på hvordan dagens kull og koks brukt i reduksjonsprosessen av kvarts kan erstattes med et bærekraftig alternativ for fremtidig produksjon av silisium. Dette har startet et forskningssamarbeid med SINTEF hvor et av fokusområdene omhandler bruk av trekull som reduksjonsmiddel. Målet med denne oppgaven har vært å simulere fremstillingen av trekull fra treflis gjennom en termisk prosess kjent som pyrolyse.

Oppgaven tar for seg numeriske strømningsberegninger (CFD) hvor masse- og varmetransporten har blitt studert. Studie av relevant litteratur og forenklinger har muliggjort en numerisk simulering av pyrolyse. En viktig del av oppgaven har vært å finne de riktige egenskapene til treflisen som skal konverters termisk til trekull. Disse egenskapene har deretter blitt overført til de numeriske modellene som hvis oppgave har vært å definere et porøst domene. Modellene har vært bygd opp av 4 steg, hvor hver av dem er CFD modeller som gradvis øker i kompleksitet. Resultatet har vært fire modeller som demonstrerer hver sin oppgave. Modellene har vist at gode tilnærminger av pyrolyse, hva angår masse- og varmestrøm, kan bli demonstrert uten å involvere kjemisk kinetikk. Resultater viser til at akkumulert masse som har forlatt reaktoren under prosessen er omtrent 75% av den opprinnelige massen. Opphetningstiden tar omtrent 100 minutter før man kan se en tilnærmet konstant temperatur i biomassen. Videre viser resultatene at et trykkfall gjennom det porøse domene er forsvinnende liten. Masse- og energibalanse har blitt utført på systemet. Beregningene viser at konserveringslovene er tilfredsstilt for stasjonære strømninger, men at i modellene må mer arbeid må til for å forbedre konserveringslovene for transiente strømninger.

Acknowledgements

This thesis would never be completed without the support and invaluable insight from my supervisors, Terese Løvås Head of Department of Energy and Process Technology at NTNU and Per Carlsson Research Manager at SINTEF Thermal Energy. To them I owe a great gratitude for their inspiration, source of motivation and patience.

This work is a token of gratitude directed towards my family, dear friends and co-students who always believed in me, prayed for me and encouraged me. A lot of thanks for all the support.

Trondheim
September 10th, 2019
Abel Mussie Amar

Table of Contents

List of Figures

List of Tables

Chapter 1

Introduction

1.1 Background

Increased efforts to reduce global greenhouse gas emissions materializes. Most notably, in December 2015, the 21st Conference of the Parties (COP21) introduced the Paris Agreement, which is an agreement within the United Nations Framework Convention on Climate Change (UNFCCC). Of a total of 197 countries, 195 have signed the agreement, [23] of which 185 parties have ratified. On a superior level, the Paris Agreement consists of articles that categorically describe methods the parties are required to use in order to create the framework for transparent financial flows towards a sustainable future, combat anthropogenic carbon emissions, and support areas in developing countries in adapting to climate change [69]. To eradicate the surplus of carbon emissions, Article 2, 1a. aims to reduce global CO2-emissions by maintaining the increasing global average temperature to be below 2^oC above pre-industrial levels and limiting the average temperature increase to be 1.5^oC above pre-industrial levels with the goal of reducing the effects of climate change. [59]

Article 2, 1a., colloquially known as "the 2-degree target", ultimately commits the participating parties to enhance emission reduction and to combat climate change through nationally determined contributions (NDCs) [20]. The European Union's strategy to meet this target, set by the EU Climate Action, will be a 40% decrease of greenhouse gas emissions by 2030 compared to the 1990 levels[24]. The EU, itself, has created a long-term strategy of an 80-95% reduction by 2050[25].

Norway, as an EEA-member, is in affiliation with the EU climate policies and its Emission Trading System (ETS)[35]. The EU ETS is a quota-based system that sets maximum limits of greenhouse emissions of certain economic sectors and plans to gradually reduce these limits overtime [26]. The EU ETS comprises approximately 50% of Norway's total greenhouse emissions [22], mainly consisting of the Norwegian land-based and offshore industry. In addition to their commitments and co-operation with the EU, Norway has created plans to reduce carbon emissions domestically and globally by 30% relative to its own 1990 level by 2020. By 2030, Norway plans to reduce 40% of its emissions. By 2050, it is adopted into law that Norway will become a low carbon society by reaching an 80-95% reduction of carbon emissions[21]. As far as the industry is concerned, this requires rapid technological development, and fossil fuel dependent companies will be required to

reduce or eliminate their fossil CO2 emissions, as well as adjusting their value chain to a greener profile.

This report will focus on the Norwegian metallurgical process company Elkem ASA. The silicon extraction plants of Elkem ASA, is immediately affected by COP 21's sustainable goals, given that the vast majority of Elkem's CO2 emission derives from fossil fuel in terms of coke and charcoal. Currently, Elkem's silicon producing furnaces extract raw silicon from quartz (SiO2) through a reduction process, in which the quartz is mixed with fossil coke and charcoal in an electric arc furnace. When charge is applied, a reduction process occurs and the quartz is reduced into pure silicon. The oxygen then binds to the carbon, forming CO. Principally, the quartz is reduced in accordance with Eq. (1.1)[30][85]. Other elements are however present particularly in the reduction agent making the complete reduction process more comprehensive. In 2018, the total carbon emissions associated with Elkem's plants in Norway is estimated to 2.6 million metric tons [34].

$$SiO_2 + 2C = 2CO \tag{1.1}$$

In 2015, Elkem initiated a strategic plan to achieve COP 21's goals called the Carbon Neutral Metal Production (CNMP). The main aim of this program is to achieve carbon neutral metal production using an optimized production process that will produce silicon from sustainable biomass and regenerate its own electric power demand through waste heat recycling processes. In accordance with Norsk Industri's ambitions, Elkem's defined goals are set to 20% and 40% reduction of fossil carbon emissions in 2020 and in 2030 [33]. Together with SINTEF, Elkem initially laid the groundwork to determine its energy demand and potential output through mass and energy balance considerations. As the proof-of-concept successfully ended in 2016, the Research Council of Norway granted a new program to proceed with additional funding for the time period 2017-2021 [46]. This program is called the "Pyrolysis of wood optimized for production of energy and tailor-made biochar for silicon production (PyrOpt)". Elkem's vision as a sustainable silicon producer is illustrated in Fig. 1.1

There are mainly two important benefits by choosing biomass as a reducing agent: sustainability and environmental reasons. Done correctly, biomass can be cultivated at a higher rate than it is consumed, making it sustainable unlike fossil carbon and coke. Furthermore, the carbon emissions associated with the reduction process are considered carbon neutral because the biomass is a part of the current carbon cycle, i.e. there are no added emissions. Also, from Fig. 1.1 it can be seen that the gas and liquid pyrolysis products play an important role for the carbon neutral scenario. As the next big step, PyrOPT will investigate how pyrolysis of biomass can make the value chain viable, as the margins for commercial success might lie on the technology for the pyrolysis and reduction process.

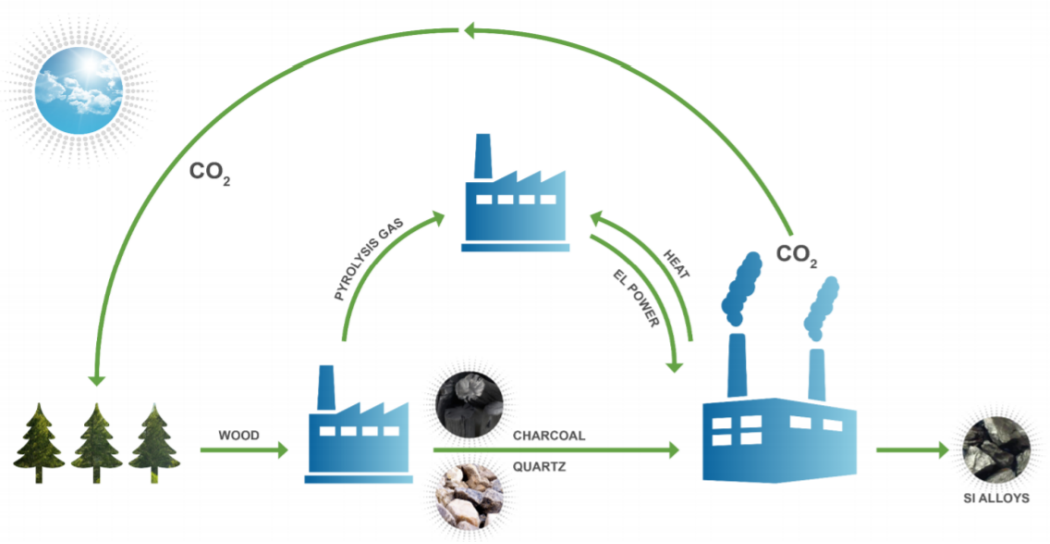

Figure 1.1: Carbon Neutral Metal Production

1.2 Problem Description

The main goal of this thesis is to uncover the heat and mass transfer phenomena that occur in biomass pyrolysis. Pyrolysis of biomass is a process by which biomass feedstock is thermally degraded into biochar (solid), bio-oil (condensate) and biogas (gas) in the absence of oxygen. In this context, the biomass used is dry pine wood chips. The approach is to model the pyrolysis numerically with a Computational Fluid Dynamics (CFD) simulation in a step-wise manner. ANSYS Fluent version 19.0 has been used to simulate these transport phenomena, a numerical solver using the Finite Volume Method (FVM). The environment in which the simulation takes place is inside a pipe furnace, or a reactor, which is a 1:1 scale CAD-model of the pipe furnace located in the Department of Energy and Process Engineering's laboratory. The reactor itself is enclosed by a heating cabinet able to heat the interior to a specified heating rate. The volatiles that emerges from a heating process would then be received by a connected unit ready to analyze the results. A depiction of the experimental setup that is to be simulated can be seen in Fig. 1.2.

The frame of work has been to model a heating process of $13^oC/min$ from room temperature to 500^oC. Wood chips of the pine wood species was the biomass undergoing the heating process. The reactor was the environment in which the process took place.

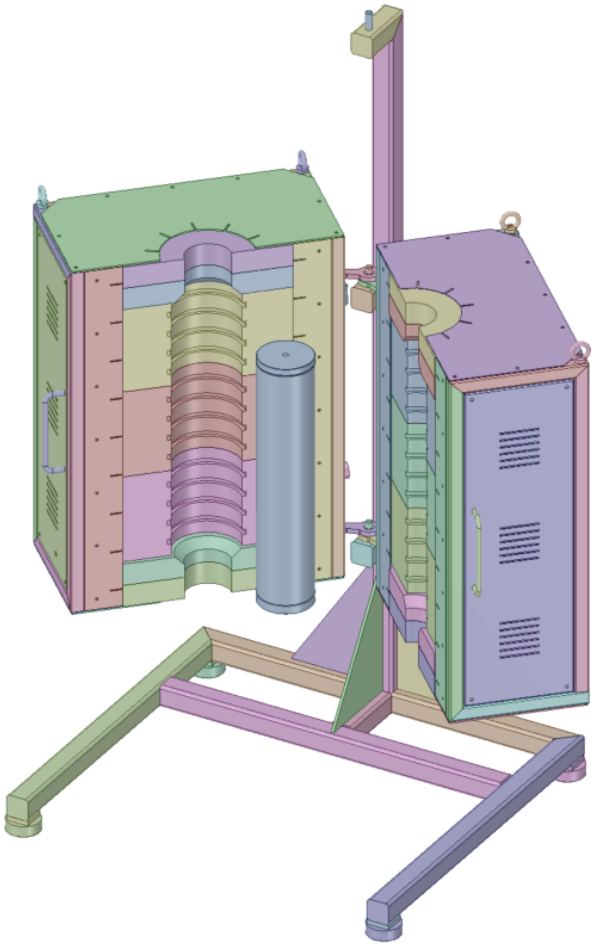

Figure 1.2: The reactor with open heating cabinet

Chapter 2

Theory

2.1 Composition of Biomass

A thermomechanical process has to take place in order to convert biomass, such as raw wood, into biochar. This literature review has centred its attention to the qualities of pine wood, in particular scots pine (Pinus sylvestris). The process that is being researched by SINTEF and Elkem is pyrolysis. Pyrolysis is the chemical decomposition of organic materials through the application of heat[16]. In this process, the biomass undergoes a high temperature treatment in the absence of air, resulting in a decomposition of existing inter-molecular structures and a formation smaller bonds.

For pyrolysis purposes, the composition of biomass is usually described quantitatively in three ways: Ultimate analysis/elemental analysis, proximate analysis and by bulk proportions. Ultimate analysis describes the biomass by the representation of its elements. It is determined by standardized testing such as the DIN EN 15104:2011 standard (Solid biofuels - Determination of total content of carbon, hydrogen and nitrogen - Instrumental methods) [28]. Proximate analysis characterizes biomass by its fixed carbon, volatile, ash and moisture content. Volatile matter is determined in a similar fashion, i.e. via standardized testing such as the ASTM E872 (Standard Test Method for Volatile Matter in the Analysis of Particulate Wood Fuels)[10]. Ash content denotes the collection of the inorganic compounds, in the form of metals and minerals and the unpyrolized biological matter. Primarily, inorganic compound are silica, aluminum, iron, and calcium [12]. In addition, biomass can also be characterized by its ligno-cellulosic composition, meaning by its main constituents that are the organic compounds cellulose, hemicellulose and lignin. The organic compounds are found in the cells walls, and together they make up for the structural integrity of the plant [13]. From Sjöström's research, it can be deduced that the main constituents cellulose, hemicellulose and lignin tend to be in the range of 0.40-0.45, 0.20-0.30 and 0.26-0.32 in terms of mass fraction respectively[71]. Huge variations exist, however, as pointed out by Miller and Bellan, in which the mass fractions can be found to be 0.22-0.50, 0.27-0.47, 0.17-0.45 for cellulose, hemicellulose and lignin respectively[57]. Table 2.1 reveals the chemical composition for a selected choice of experiments. Naturally, as the sample species vary from the experiments, the ultimate and proximate analysis will yield unique results. In the first experiment, by Gonzaléz et al., the sample specimen is wood chips from the

species Jacaranda copaia. Sensöz and Can used wood chips from a mix of pine species, Wang et al. used white pine and Grønli used scots pine. As the name implies, it should be noted that in proximate analysis, the fixed carbon content, volatile matter and ash content are only proximate values, as the true yield depends on how the experiment was carried out.

Table 2.1: Biomass composition from selected experiments

Components, wt%	Gonzalez et al. [36]	Sensöz, Can [68]	Wang et al. [79]	Grønli [40]
Proximate Analysis				
Volatiles	89.92	87.04	81.01	87.6
Fixed carbon	8.67	12.61	11.98	12.3
Ash	1.41	0.35	0.95	0.1
Moitsure		7.40	6.06	
Ultimate analysis				
C	49.88	46.08	49.44	46.9
H	7.35	5.29	6.33	6.3
O	41.08	48.41	43.85	46.7
N	1.52	0.22	0.38	0.07
S	0.17			

2.2 Pyrolysis of Biomass

The pyrolysis process can once more be categorically divided into different processes, depending on the operating conditions. Principally, variables such as heating rate, residence time of the versatile vapor inside the bed reactor and final temperature determines the type of pyrolysis [11]. The purpose is typically to produce either organic solids (biochar), liquids (tar, condensate) or gas (wood gas), depending on the process used. Typical processes include, but are not limited to, conventional pyrolysis, fast pyrolysis and flash pyrolysis[14]. However, it is not always a simple task to determine the pyrolysis process qualitatively as the criteria for operating conditions are not imperative. To optimize the biochar yield, conventional pyrolysis is the most convenient as longer residence time allows the volatile matter to form solids[29]. The principal parameters for pyrolysis can be seen in Table 2.2. Conventional pyrolysis, or slow pyrolysis, is the heating process that is to be modelled numerically.

In a review paper authored by B. V. Babu, the heat transfer mechanisms along with the chemical kinetics during pyrolysis were describes in 5 steps[11]: temperature increase of the fuel driven by a source of heat (1), the pyrolysis initializes with the release of volatiles simultaneously with the formation of char (2), outflow of volatiles resulting in a bulk transport of heat to cooler areas (3), condensation of the gas and formation of tar (4), autocatalytic secondary pyrolysis as a result of interactions (5).

Table 2.2: Main operating parameters for pyrolysis. Source: Babu [11]

Pyrolysis parameter	Conventional pyrolysis	Fast pyrolysis	Flash pyrolysis
Final temperature [K]	550-950	850-1250	1050-1300
Heating rate [K/s]	0.1-1	10-200	<1000
Particle size [mm]	5-50	<1	<0.2
Residence time [s]	450-550	0.5-1.0	<0.5

Steps 2 and 5, that is the chemical reactions, are known to be the primary and secondary reactions as described by Ström and Thunman[72]. When ligno-cellulosic materials are heated to temperatures over 200 ^{o}C[48], the primary reactions form in which gas development consisting of water vapor and light gases such as CO_2, CO, H_2, CH_4 and light hydrocarbon[39][29] gases takes place, as well as primary char and tar formation. Fig. 2.1 demonstrates a simple overview of primary and secondary pyrolysis reactions typically used in pyrolysis modelling. Volatiles consist of both condensable and non-condensable products. Rath et al. investigated the heat of pyrolysis by conducting experiments on beech and spruce and found the heat of primary pyrolysis to be endothermic[65]. According to Milosavljevic et al., primary reaction is said to be endothermic as it is associated with the latent heat of vaporization of the volatile vapors [58]. Secondary reactions is more complex, and poses more difficulty to quantify since it spans a number of various intermediate reactions. The gas and liquid produced by primary reactions initiate the secondary reactions, e.g. cracking, reforming, dehydration, condensation, polymerization, oxidation, and gasification[60] due to reciprocal interference and with the solid carbon, producing secondary gases and char. The final pyrolysis products are considered to be formed by both homogeneous reactions from the volatile materials, and heterogeneous in contact with the solids[14].

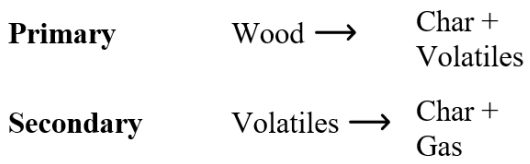

Figure 2.1: Simplified overview of reaction mechanisms

Furthermore, it is concluded that secondary pyrolysis is exothermic and indicated it being a factor to cause experimental variability[65]. It has also been using as a unknown variable in modeling studies - adjusted to make it agree to experiments [43]. It is suggested a reason for this might lie in the autocatalytic effects of the volatiles and the impurities, i.e. the inorganic compounds. Grønli summarizes the heat of pyrolysis by stating that with the absence of air and impurities, the pyrolysis is purely endothermic. Exothermic reactions occur in greater sample sizes and with the possibility for the volatiles to react[40]. The magnitude of reaction heat ranges greatly. The difference is attributed to factors such as: experimental method, conditions of pyrolysis and composition[70].

The heat of reaction is reported to lie in the -2100kJ/kg to 2500kJ/kg range[58].

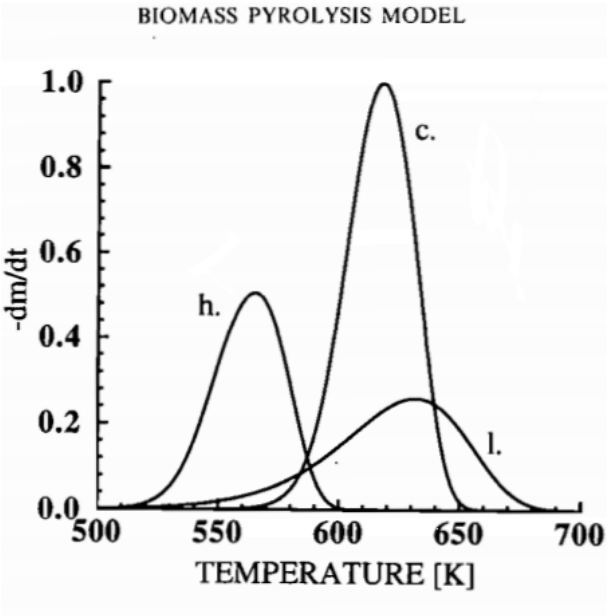

Figure 2.2: Normalized DTG curves of cellulose (c.), hemicellulose (h.) and lignin (l.). Source: Miller[57]

Cellulose, hemicellulose and lignin decompose at different temperatures ranges during pyrolysis. The temperature range at which each component decompose was found to vary slightly between the works of Yang et al., Sjöström and Demirbas, [84][71][27]. Yang et al. perfomed a study to investigate pyrolysis of celluloce, hemicellulose and lignin as pure synthetic substances. The mass loss was and the rate of mass loss was studied through thermograiometric analysis (TGA) differential thermogravimetric analysis (DTG). From their research it was concluded that for temperatures $<100^oC$, moisture content in reactor increases, from 220-350 ^oC hemicellulose breaks down, then cellulose at 315-400^oC and lastly lignin from $>400^oC$. The decomposition of lignin is characterized as slow from a greater range of temperatures, with no clear peak value[57][84]. Fig. 2.2 is a result of a numerical experiment conducted by Maschio et al., in which the DTG curves have been normalized with peak cellulose value as reference. In Yang et al.'s work, the same shape of the curves can be observed. In their analyses, hemicellulose is observed with a peak value of 0.07wt% at 260^oC, cellulose has a maximum mass loss rate at 2.1wt% at 355^oC while lignin is slowly decomposed during the whole process, not exceeding 0.15wt% in the experiment. While the remaining solid residue of hemicellulose and lignin was measured 20% and 7% of its initial mass respectively, the solid content of lignin was measured to about 60% . Thus the solid residue of pyrolysis is mostly attributed to the lignin content. In terms of gaseous products, a review authored by Chouhan and Sarma on the topic of bio-oil process parameters stated that hemicellulose generates high CO_2 amounts, cellulose contributes most to the CO yield and lignin was responsible for higher H_2 and CH_4 amounts[18].

As far as the biomass yield are concerned, the products of pyrolysis are generally divided into

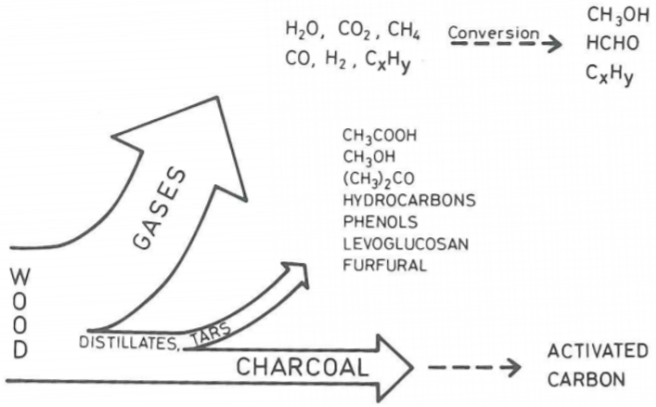

Figure 2.3: Sankey diagram of a generalized pyrolysis of wood. Source: Sjöström [71]

three: biochar (mostly carbon), condensate , tar or bio-oil (heavier hydrocarbons, liquid water) and non-condensable pyrolysis gases (CO_2, H_2O, CO, CH_4, C_xH_y). The weight percentage of the products can generally be expected to be in the range of 20-31, 21-59 and 12-23 for biochar, condensate and the non-condensable gases respectively[83][82][68], assuming pyrolysis temperature of approximately 500^oC and moderate heating rates. The products can be further divided into set of organic substances. Fig. 2.3 displays the possible substances that can be found in the volatile matter, and possible conversion routes for the char and gases. Final temperature, pressure and heating rate are considered the most important parameters for biochar optimization[29]. Various parameters also affects yield such as: composition, ash content, particle size, density and moisture content[**needed**]. A generalized pyrolysis equation of reaction for biomass can be describes as[14]:

$$C_nH_mO_p(biomass) \xrightarrow{heat} \sum_{liquid} C_xH_yO_z + \sum_{gas} C_aH_bO_c + H_2O + C(char) \tag{2.1}$$

In which n, m, p and x, y, z, and a, b, c, denotes the mole quantity in the biomass, liquid and gaseous products respectively. Eq. (2.1) assumes that biomass entirely consist of carbon, hydrogen and oxygen. From what was observed in Table 2.1, traces of inorganic elements, lumped into the ash category, can be found. The ash content has proven to influence the product yield as a catalyst, however they generally do not participate in the chemical reaction.

Biochar is a highly porous substance with a very high carbon content usually being more than 85wt%[14][9] and is produced in relatively low temperature ($>700^oC$)[55] and heating rates[83]. Biochar is very similar to fossil coal in general, the main differences can be seen in the its lower amounts of nitrogen and ash content, thus making char derived from biomass more pure[9] in terms of carbon content. Due to its porous structure, a high reactivity is associated with biochar making it a very attractive chemical precursor. Its inherently high porosity increases the surface area of soil making improving the soil's water retention abilities. For the same reasons, it has been used to filter air and water impurities. Biochar can be upgraded to activated carbon which is essentially a more porous substance, higher surface area, reactivity and other improved qualities[44][66]. Biochar is also

considered a carbon neutral solid fuel used in co-firing together with fossil coal to reduce enhanced carbon emissions. In 2017, Elkem replaced 20% of its fossil carbon content with sustainable biomass, reaching its 2020-milestone 3 years in advance[32]. Biochar yield can be optimized with catalysts. The biochar amount has been reported to increase when catalysts such as Na, K, Ca, Mg, and Cd are present during the process[18].

Tar, or bio-oil, is a complex mixture of organic compounds. Tar is a collective term that consisting of water and various functional groups such as acids, sugars, alcohols, ketones, aldehydes and phenols[14][79]. The heating value of tar can be found to be 14-18 MJ/kg which is generally lower than that of dry biomass or char. Therefore it is more preferred as a fuel for drying processes or heating rather than power generation. Pyrolysis processes with low residence time and high heating rate is beneficial for the bio-oil production as the volatiles can escape the reactor prior to substantial char formation. An immediate condensation is then important before it further decompose to smaller compounds[14]. For longer residence times, the volatiles produced from the primary reactions are likely to undergo char-induced cracking in which secondary char and light hydrocarbon gases are produced[72].

The gas yield comprises the non-condensable fluids as a result of primary and secondary reactions. It is also termed wood-gas, syngas or biogas. Gas yield is maximized in pyrolysis processes with short residence time, high pyrolysis temperature and rapid heating rate, i.e. during flash pyrolysis or gasification processes[83]. The majority of the gas is a mixture of CO_2, CO, H_2 and CH_4. In addition, small amounts of light hydrocarbon gases exist such as ethane, ethylene, propane, propylene which was found in Grieco and Baldi's experiment of pine wood pyrolysis[39]. The experiment estimated the C_2 and C_3 hydrocarbons to be 2.1 volume %, which will make the said hydrogen and hydrocarbon gases to account for 97.9%. As shown in a experiment conducted by Wang et al., the gases are formed during different stages of pyrolysis. The experiment, which consisted of 5 runs using constant and variable heating rates between 2 and 20 ^oC/min, showed that CO_2 is formed slightly before CO with almost the same mass loss rate, thereafter CH_4 and lastly H_2. The result of the constant 9.2 ^oC/min run is illustrated in Fig. 2.4. The curves show that it is in good accordance with the decomposition hemicellulose, cellulose and lignin mentioned earlier.

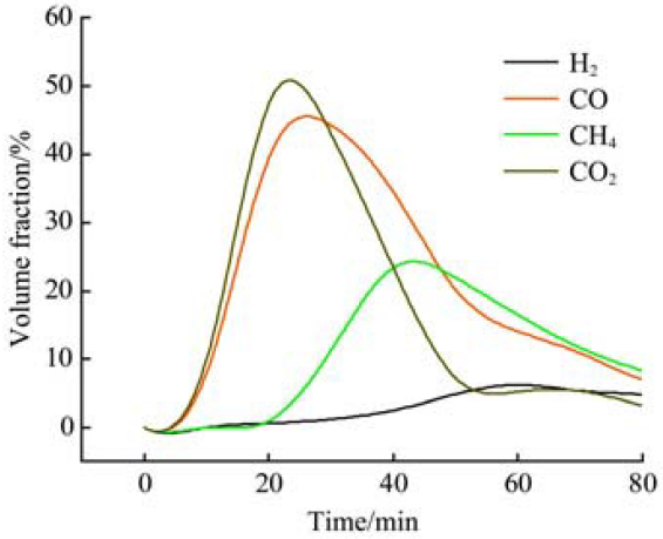

Figure 2.4: Distribution of gases from pine wood. Source: Wang et al.[79]

Physical experiments from the literature study has been retrieved to create an overview of wood pyrolysis with similar traits. The findings that can be found in Table 2.3 displays the operating parameters as well as the yield products. Sweep gas was not used in any of the runs and there were no presence of catalysts. The results found in Table 2.3 summarizes data that will provide the basis for the method and material selection.

Table 2.3: Comparisons of product yield from experiments on woody biomass

Measurement [units]	Wu et al. [82]	Sensöz, Can [68]	Wang et al. [79]	Williams, Besler[80]
Operating parameter				
Sample	Sawdust	Turkish pine	White pine	Pine
Heating rate [^{o}C/min]	20	7	9.2	20
Final temperature [^{c}C]	520	500	520	420
Particle size [mm]	1.5	4.5	5-6	10
Yield [wt%]				
Char	22.12	27	27.37	26.4
Liquid	59.09	23	54.82	46.0
Gas	18.79	14	17.81	27.6

Chapter 3

Methods and Materials

3.1 Numerical Tasks

The goal of this thesis is to model a pyrolysis process of woody biomass using CFD to investigate the heat and mass transfer mechanisms during the process. The framework conditions that makes the basis of this exercise is the pipe reactor depicted in Fig. 1.2. The sample material of this simulation is aimed to share the same characteristics of wood chips of the species Scots pine to the extent it is possible. The sample wood is contained in a fixed bed reactor situated in which the whole setup is located in ambient temperature and pressure. For this master thesis, the following numerical tasks will be done:

- Transient simulation of an empty pipe furnace with a uniform gas source term
- Transient simulation of a pipe furnace with porous media or equivalent representing biomass with a gas source term
- Transient simulation of a pipe furnace with porous media or equivalent with a gas source term which is temperature dependent
- Transient simulation of a pipe furnace with porous media or equivalent with a gas source term which is temperature dependent and inlet of cold inert gas from the bottom of the reactor

The 4 tasks will respectively being referred to as case 1, 2, 3 and 4. The purpose of the steps is to arrive to a simulation which is understandable, precise and efficient. In case 1, the mass source represents the gas development that will occur during pyrolysis. The first step will be to model the gas without the biomass. The mass source will be a constant source term, with a temperature that is temporal and spacial coincident with the temperature inside the reactor. Following, case 2 incorporates the biomass in the simulation which is to be modelled as a porous medium. The biomass is created as a porous region to account for the dense packing of the loose wood chips in the reactor. Case 3 continues from case 2 by changing the constant mass source into a temperature dependent variable according to the mass loss rate of the wood during a pyrolysis. Case 3 will be

the last step to simulate a complete pyrolysis process. Lastly, case 4 is a simulation that contains purging of the biomass and the volatiles.

A computational fluid dynamics (CFD) analysis is normally divided into the following steps: creating the computational domain, dividing the domain into a finite number of elements, define properties and boundary conditions and solving with suitable numerical schemes and lastly extraction and processing of the results. The steps can be categorized into the stages preprocessing (first two steps), solution (the following two steps) and post-processing (the last two). This thesis aims to follow the steps accordingly.

3.2 Assumptions and Limitations

Assumptions are made to facilitate the simulations. The following list describes the assumptions that were made in prior to the simulations. These assumptions apply to each of the cases:

1. Simulations are done without a chemical kinetics model. In addition, the latent heat of vaporization from a solid or liquid to gas phase is not included.
2. The volatiles, the liquid and gas phase, will be modeled as pure gas phase. Secondary reactions such as condensation or cracking inside the reactor will not be a part of this simulation.
3. The conduction through the steel walls of reactor is not included. The boundary conditions are set on the fluid domain, i.e. on the inside of the pipe walls.
4. The flow problem is assumed to be axisymetric along the center line of the pipe furnace. Thus, swirling flow is not accounted for.
5. Constant thermal properties of biomass has been used. The propertied include density, specific heat capacity, thermal conductivity, and porosity.
6. The thermal expansion due to the heating of wood is neglected.

Some limitations are associated with these tasks. The limitations in this thesis are considered to be:

1. The collected biomass properties from literature study differ slightly from each other. A final guess had to be made.
2. When transferring material properties reviewed from literature to a simulation software, not all details about wood chip geometry and properties in general are considered.
3. The mesh grid of the geometry is divided into a discrete number of elements, same goes for the discretized fluid flow equations, so there will always be a numerical error involved in the analyses.
4. The deadline of this thesis limits the amount of time put into this work.

3.3 CAD Model

The preprocessing began with a redesign of the 3D-geometry of the pipe furnace. ANSYS' geometry editor Spaceclaim version 19.0 was used. Initially, a volume of fluid had to be created from the CAD model as it consisted of solid surfaces and bodies solely. The computational domain for this CFD simulation will be the interior of the reactor. This body of fluid was created with the tool function "Volume Extract". The 3D design was modified into an axisymmetric 2D design. This was done by first cutting the cylindrical volume of fluid horizontally into 4 equal parts. Thereafter, 3 parts were removed. Finally, a 2D contour was drawn on top of the remaining 1/4 part and a surface was created from it. A 15mm narrow tube on top of the geometry was kept for the gases to exit. With the "Split Body" tool, body sections were created to separate the parts of the fluid volume from each other to prepare the geometry for meshing. The body was split into 4 regions (5 for case 4). The regions are separated by a dividing line which can be viewed in Fig. 3.1 A last function called "Share Topology" was used to tell the program that it is still one body consisting of different parts. This facilitates the meshing process as it will not be necessary to define a interface mesh between the sections later on. In order to use Fluents's 2D axisymmetric analysis type, the center line of the CAD model had to be aligned right on to the x-axis of the geometry model's global coordinate system. The bottom was chosen to be placed on the origin, while the top of the body lies on the positive x-axis. For Case 4, a small adjustment was made to the new geometry. A small tube inlet, matching the size of the 0.48 inch radius from the top, was made to accommodate for the purge gas inlet. The length of the tube is 10mm. The initial and final geometries can be view in Fig. 3.1.

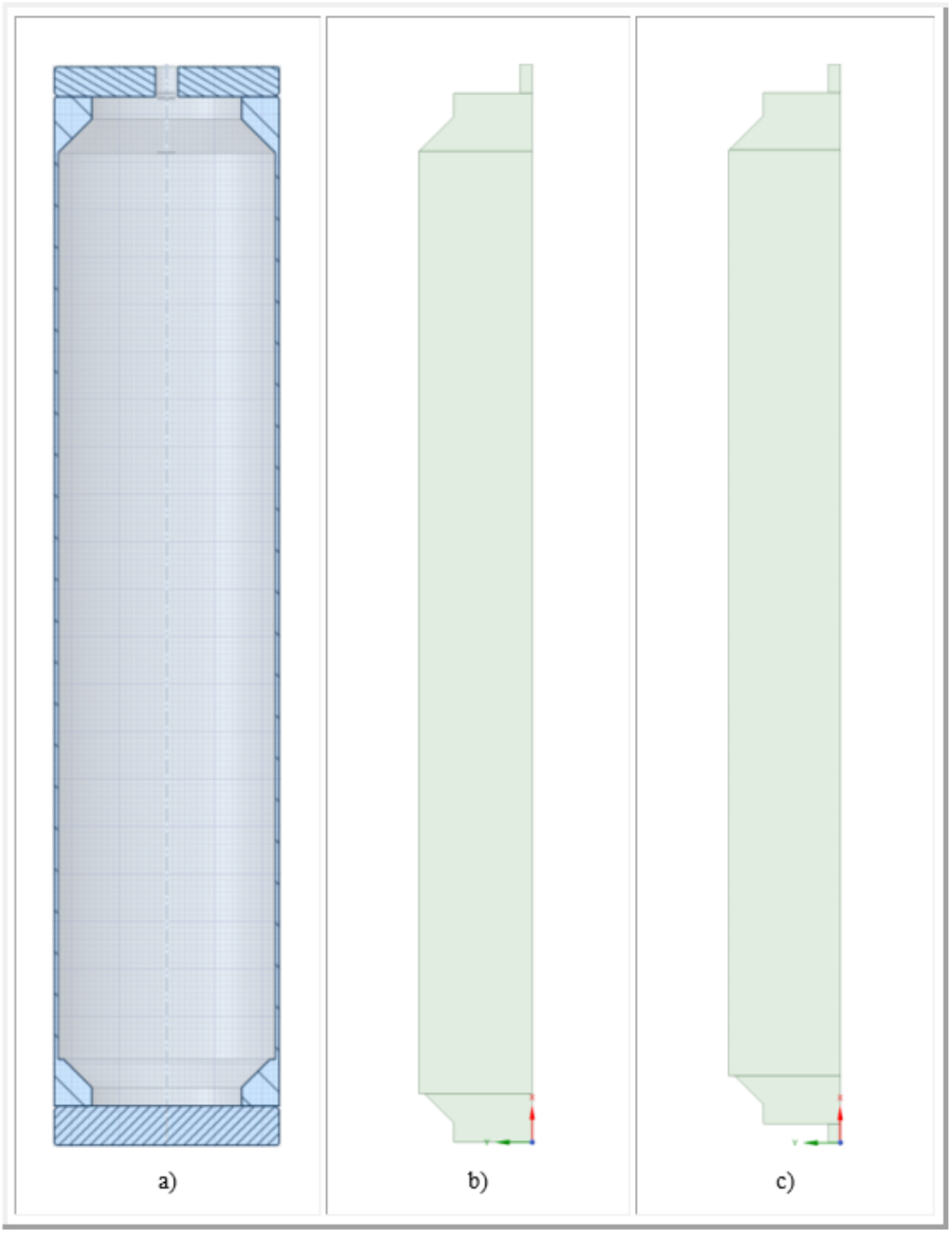

Figure 3.1: Display of: a) Initial 3D geometry consisting of a solid tube with a cavity inside. b) 2D axisymmetric geometry with origin placed at the bottom. Red and green indicates x and y coordinate axes respectively. c) 2D axisymmetric geometry with added gas inlet.

The key dimensions of the reactor play an essential role in the numerical simulations. A sketch of the CAD model including its most important measurements for the first 3 cases can be seen in Fig. 3.2. The corresponding values to the parameters is listed in Table 3.1. Volume and surface area calculations used a cylindrical 3D geometry to arrive to the listed values. Regarding case 4, the parameters L_1, L_2, V_1 and V_2 has taken the gas inlet into account. Furthermore, D_1, and evidently A_1, is equal to the diameter of the inlet. Technical drawings of case 4 can be seen in Appendix A.

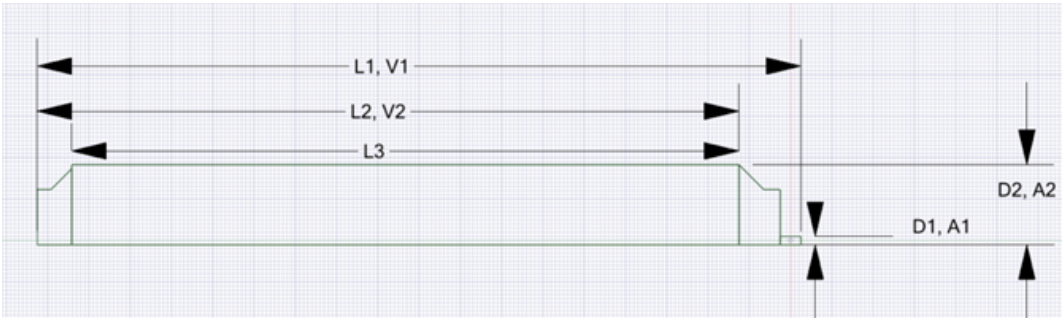

Figure 3.2: 2D sketch of the computational domain with measuring lines and parameters that was used in the first tree cases.

Table 3.1: Values of key geometric measurements

Measurement	Parameter	Cases 1-3	Case 4
Diameter [mm]	D_1	12.2	12.2
	D_2	58	58
Length [mm]	L_1	555	565
	L_2	510	520
	L_3	485	485
Area [mm^2]	A_1	116.8	116.8
	A_2	10568	10568
Volume [mm^3]	V_1	$5.482e+06$	$5.482e+06$
	V_2	$5.283e+06$	$5.284e+06$

3.4 Domain Discretization

The preprocessing continued by discretizising the fluid domain. Meshing is the process in which the continuous physics of the domain becomes discretized into a finite number of cells, also known as elements. A summary of the mesh review has been synthesized to a table that include some important metrics. The summary is listed up on Table 3.2.

The philosophy of the meshing process has been to find the most suitable combination of quality, stability, accuracy and efficiency. Efforts were made to create a mesh that is of good quality (ideal

Table 3.2: Element statistics of some important features

Metric	Cases 1-3	Case 4
Number of elements	31047	30785
Number of nodes	31785	31543
Skeweness		
Average	5.160e-002	5.621e-002
Standard deviation	8.464e-002	8.902e-002
Orthogonal quality		
Average	0.992	0.991
Standard deviation	2.575e-002	2.675e-002

shape) to make sure that a stable and accurate solution is obtained. Moreover, the process also aimed the mesh to be refined to an appropriate extent such that an accurate solution can be obtained. A fine mesh is needed to resolve high solution gradients and geometric details, while coarser mesh can be used elsewhere. However, too many elements risk the numerical model to be inefficient, and it is also possible that there are so many elements present that the solution will not change if the number of elements is reduced. Having too many, or small, elements affect the setup of the transient cases. Smaller elements require smaller time steps according to the Courant-Friedrich-Lewy (CFL) condition, as will be discussed later.

ANSYS Meshing version 19.0 was used to produce the mesh. Principally, 4 meshing techniques were used to create the model. On a global scale, the mesh sizing and growth rate functions were used. The maximum limit of the element size was set to 1.1mm. Rate of growth from smaller to bigger elements was set to 1.2. On a local scale, edge sizing and face sizing were made to adjust the mesh. Edge sizing was implemented along the edges of the domain except for the axisymmetric edge and the outlet edge. The edge sizing was set to 0.5mm. The purpose of the edge sizing is to refine the mesh networks as high solution gradients are expected to occur along the solid-fluid interface. Because the walls of the pipe furnace transfer heat and induce convective heat transfer it is vital to capture both the physics of the thermal and the velocity boundary layer. The edge sizing approach was favoured over creating inflation layers as the edge sizing method proved to be more refined around small corners and faces. The y+ approach, which determines the minimum cell size from a solid surface, was also not used as a laminar flow regime will be used in the flow simulation. Finally, for the inlet and outlet surfaces the faze sizing was set to maximum 1mm. The mesh can be viewed in Fig. 3.3. Similar results and statistics for case 4 can be viewed in Appendix B.

The produced mesh shows an unstructured network that is more refined in along the walls on the left hand side. That proves to be beneficial as this side of the domain is supposed to be a fluid-solid interface, thus high solution gradients are expected to occur here. It it also important that mesh in the outlet tube is slightly more refined than the rest of the domain. From Fig. 3.3 it shows to be true, with approximately 8 elements across the radius. By a visual inspection on the interface between the regions, it can be determined that it looks satisfactory. The next step was to review the mesh metrics and quality.

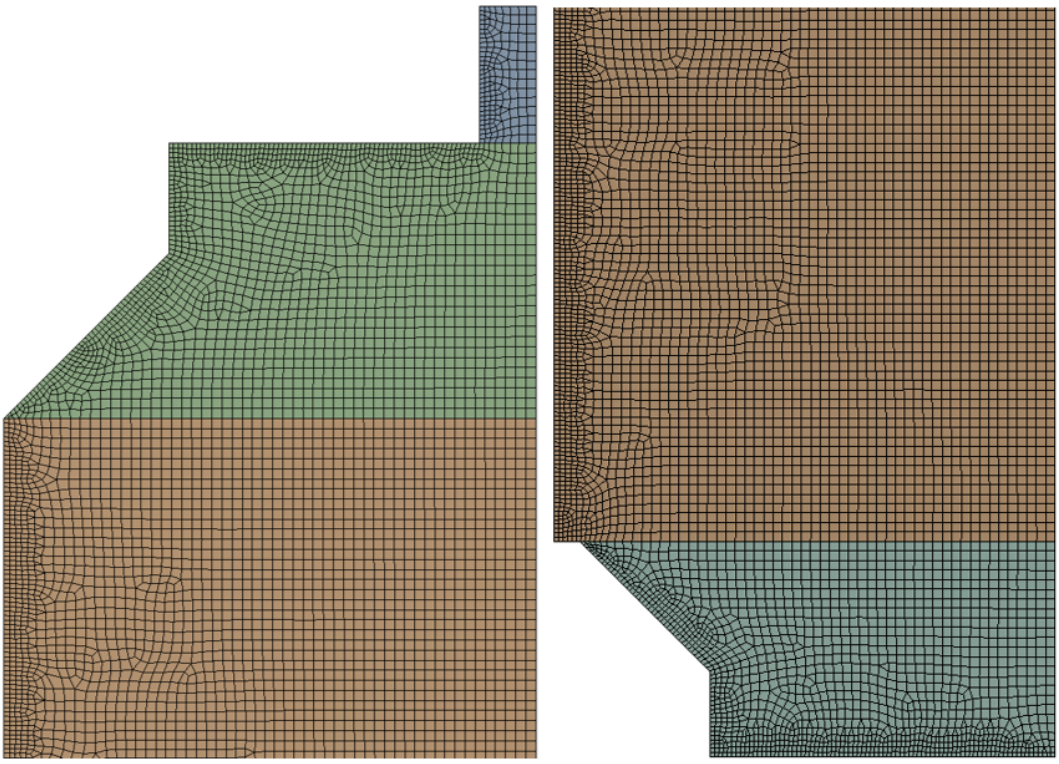

Figure 3.3: A side-by-side of the discretized domain with the top to the left and bottom to the right.

The nodes and elements number was calculated to be 31785 and 31047 respectively. Just over 31000 nodes and elements is usually not considered an alarming amount. A check to see how many elements this would be for a 3D geometry with exactly the same conditions showed that the element count was no less than roughly 50 million elements (Appendix B). The vast difference just proves how much computational costs can be saved by opting for a axisymmetric analysis.

The mesh quality had to be checked to see if any adjustments were necessary. To review the quality of the mesh, the skewness and orthogonal quality of the mesh were examined. In brief, skewness describes the degree of distortion relative to the ideal shape of the element. An ideal shape is considered as the angle that would make a triangle equilateral and a quadrilateral equiangular. Maximum skewness is taken to be 1, while a perfectly equilateral triangle or equiangular quad would have a value of 0. Orthogonal quality is a quantitative representation of the alignment of the centroids of an element to the next. It measures how well the elements are placed next to each other. Orthogonal quality ranges from 0-1, in which a perfect alignment is taken to be 1 and worst possible orthogonality is 0.

Fig. 3.4 illustrates the skewness of each element through a bar chart. The vertical axis shows the number of elements, while the horizontal axis displays the skewness. As the figure shows, two element types are present. A vast majority of the elements are quads, while triangles make up for the rest. With approximately 30000 elements being less than 0.20 and the average skewness is

calculated to be 5.16e-002 with a standard deviation of 8.46e-002, it can be determined that the quality of the mesh in terms of skewness is very good. Results show to be quite similar as far as the orthogonal quality is concerned. By studying Fig. 3.5 it can be determined that it is of high quality. The average is 0.99172 with a standard deviation of 2.57e-002.

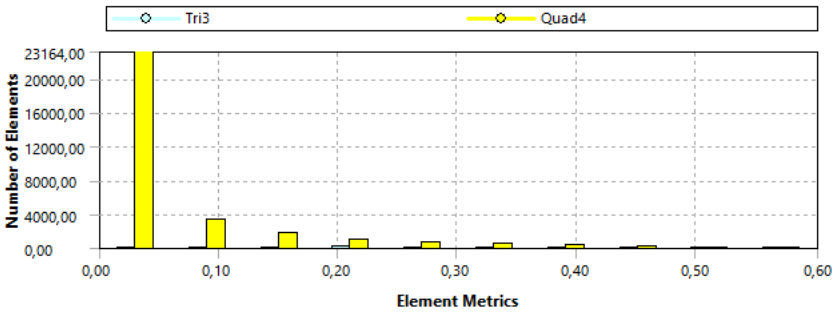

Figure 3.4: Skewness for the first geometry.

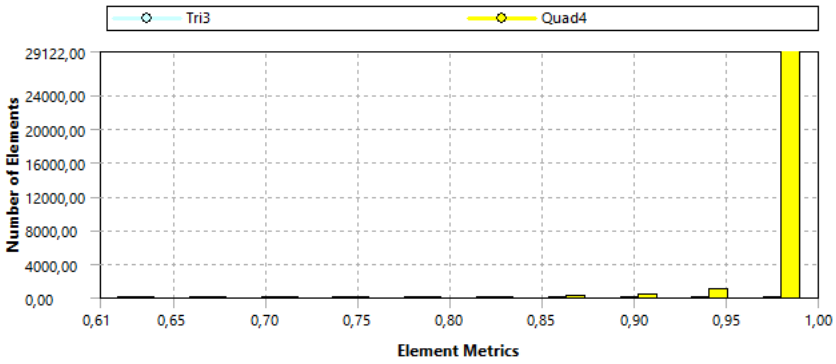

Figure 3.5: Orthogonal quality for the first geometry

Naming the faces and edges was the last step of the meshing process. The geometry was split into 4 main regions during the CAD modeling, and from these separations it is possible to name regions by convenience. The names will reappear in the boundary and cell zone conditions. It is therefore important to select correct fragment of a line or face in order to create the correct boundary or cell zone condition. The named selection is categorized into colour and number codes that represent faces and name of edge(s) respectively, as can be seen in Fig. 3.6. The codes have the following significance:

- Blue: Cell Zone 1
- Green: Cell Zone 2
- 1: Outlet
- 2: Top
- 3: Wall
- 4: Bottom
- 5: Symmetry

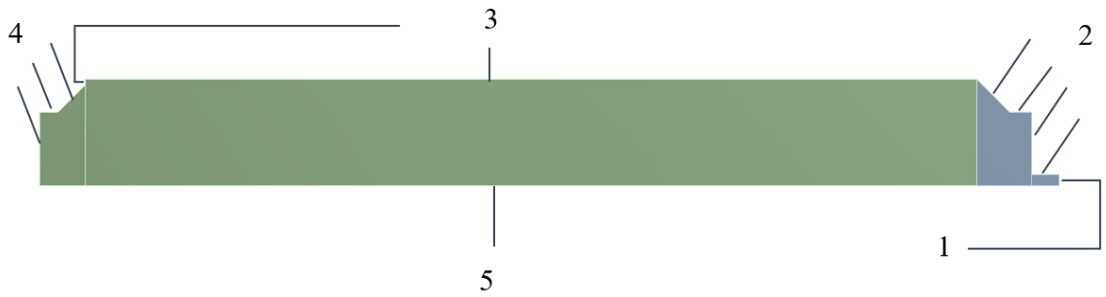

Figure 3.6: A depiction of a coloured domain with lines and number codes. The colour indicates a cell zone, lines refer to edges and numbers is the name given for the edge(s).

3.5 Material Properties

This section focuses on the choice of properties assigned to the materials that was used in the simulations. The materials involved in the scope of this thesis are wood and a gas mixture equivalent to the volatile gases. Ground wood chips of Scots pine provided the basis for the search. The choice of the thermal properties density, thermal conductivity, heat capacity and porosity along with its dependent variables will be discussed. To facilitate the simulation work, they were chosen to be of constant value although the devolatilazion will in reality gradually change towards properties that is associated with char. Heat transfer properties between the gas and solid has also been considered.

3.5.1 Wood thermal properties

Density of wood is dependent on species and moisture content mainly[31]. Specific gravity, that is the ratio of the wood sample to that of water, is usually the convention to denote density. Based on the moisture content, there are 4 main categories for which specific gravity is determined: by green density, air-dried density, oven-dried density and by oven-dry mass divided by green volume. The latter is formerly known as basic density or specific gravity. Green density is the density of newly sawn wood and is expected to have a very high water content. Air dried density has a moisture content that is in equilibrium to ambient air's humidity and is normally taken to have around 12% moisture content[17]. Oven-dried density is the density of wood without any moisture content. In the simulation work, the density of oven-dried wood chips samples was used. When stacked together, wood chips will naturally have big pockets of air occupying the space between the chips. Consequently, the density of a collective amount of wood chips in a confined space will be different from a solid wood block occupying the same amount of space. This will be further discussed. Experimental studies and wood data tables provided the insight to determine the wood density. In an experimental study of oven-dried pine wood, the density was recorded to range from 463-526 kg/m^3 with a mean of $491kg/m^3$[77]. Similarly, in a paper on thermal and electric properties of Scots pine, the average density of the wood species was said to be $470kg/m^3$ oven-dry[49]. The density was therefore taken to be 470 kg/m^3.

The thermal conductivity was decided from a empirical correlation. It was found to range from 0.11-0.22 W/mk for most types of wood[75][74]. It is said to be temperature, moisture content and density dependent [81][74], however it is not dependent on the species[37]. Thermal conductivity also depends on the orientation of the wood fibres. It is commonly known to be twice, and possibly more, as big along the fibres than across[50][64]. This trait is would be very useful for a single particle study, however when a simulation concerns hundreds of wood chips, to account for the orientation of each wood particle is highly impractical and will not be done in the simulation work.

After evaluating different correlations on thermal conductivity [64][37][50][17][15], the correlation first formulated by MacLean in 1941 has proven to be one of the most frequently used. For moisture content less than 40% the formula is expressed as

$$\lambda = (1.39 + 0,028u)G + 0.165 \tag{3.1}$$

in which λ is the thermal conductivity expressed in British thermal$_{IT}$ unit ($BTU_{IT} * in/(hr * ft^2 *^o F^1)$), u is the moisture content in percent, and G is the specific gravity of oven-dry wood. To convert into metric units $[W/mK]$, λ has to be multiplied with a factor of 0.1442. With a wood density of value, i.e. $G = 0$, the constant term 0.165 in imperial units is equal to that of air ($\approx 0.0024W/mK$). As water has higher thermal conductivity than wood, increasing amount of moisture content would result in higher conductivity. With no moisture content present however, as previously discussed, the thermal conductivity is calculated to be 0.12 W/mK from Eq. (3.1). Taking the fibre direction into consideration, one can expect the conductivity to be higher if wood chips are arranged in a random order on top of each other, leading to some chips more efficiently conducting heat in the longitudinal direction. Thermal conductivity was therefore chosen to be slightly higher, with the value of 0.20 W/mK.

A constant specific heat capacity was used for the wood as well. The specific heat of wood is the sum of the specific heat of dry wood and the water bound in the wood structure, however as far as dry wood is concerned the specific heat is considered solely temperature dependent[50][37]. Specific heat is from 0-100 ^oC considered to be linearly dependent with the form

$$cp_{0-100^oC} = a + bT \tag{3.2}$$

in which a and b are constants and T is in Celsius degrees. In a comparative review by Radmanovic[63], a and b range from 1.0841-1.5488 and 0.004202-0.005060. Based on these numbers, the specific heat would then range from approximately 1200 to 1600 J/kg^oC in 20^oC room temperature. This approach was first used despite being outside the range of validity. The goal was to arrive to a specific heat that would cover a temperature range from 20-500^oC. Therefore a temperature of 250^oC was used in Eq. (3.2) with a result of 2326 J/kg^oC[50]. It was discovered later that with no considerable water content, the value is too high and thus the relation was extrapolated too far. Fig. 3.7 shows how temperature is related to wood and charcoal specific heats. The length of curve reflects the validity with respect to temperature, except for the "wood char" curve that extends to 1990 ^oC.

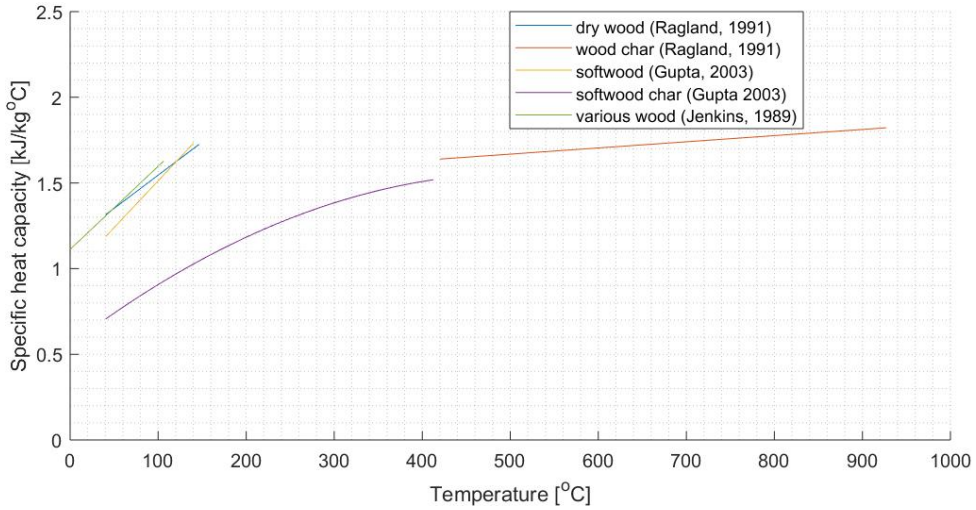

Figure 3.7: Specific heat capacities of dry wood and wood derived charcoal comparisons. Source: Ragland[64], Gupta [41], Jenkins [47]

From Fig. 3.7 it is more evident that the specific heat should be lower than $2000 J/kg^oC$. A new specific heat was decided, one that would reflects both wood and char properties at 250^oC. The novel specific heat capacity was finally chosen to be 1700 J/kg^oC.

3.5.2 Wood porous properties

The last wood property that had to be determined was porosity. The porosity of a material is defined as the ratio of the pore volume to the total volume of the material[45]. As previously mentioned, the

packing of wood chips in a container creates pockets of air, or fluid, so that the total volume of the container would be the sum of the wood chips volume and the fluid volume. In reality, the porosity of the wood chips is anisotropic, namely dependent on the alignment of the wood chips. The cylinder walls also effect the porosity as it forces the packing of the wood chips to change orientation to lie along the walls[42]. This thesis will nonetheless assume an isotropic porosity based on the following calculations. In order to calculate porosity, the following equation can be used

$$\gamma = 1 - \frac{\rho_b}{\rho_p} \tag{3.3}$$

in which γ,ρ_b and ρ_p is the porosity, bulk density and particle density[19]. In porous media, the bulk density is always higher than the particle density, and therefore is the porosity ranges from 0 (completely solid) to 1 (completely fluid), or 0-100%. The bulk density is the density of a material including its solid and pore volume, while the particle density will be the density of the only solids present which in this case will be the wood density. The bulk density was determined from the mass of the wood chips that measured 795 grams on average based on five experiments. Together with the volume V_2 from Table 3.1, which will be the porous domain, the bulk density was calculated to be $150.4 kg/m^3$. Using Eq. (3.3) with 470 and 150.4 as the values of particle and bulk density respectively, a porosity equal to 0.68 was achieved. This means the wood volume occupies 32% of the volume, while air, or gas, occupies 68%. The values seems to be in good agreement with experiments to determine wood chip porosity. Christianson et al. [19] conducted experiments that determined the porosity to be in the 66% to 77% range for wet chips typically used in playgrounds or in landscaping. Additionally, Ima and Mann[45] achieved 63% porosity for store bought wood chips that was used as a biofilter media, and a packing factor of 38% (62% porosity) was used in a numerical analysis by Gonzalez et al[36]. Values ranging from 0.4-0.8 as initial porosity has also been reported for numerical experiments[72][61][53]. It was therefore determined that a porosity of 68% was reasonable and chosen for the simulation work.

Additional input is required by the Fluent software to further elaborate the porous media formulation. Flow in porous media is associated with pressure loss. The pressure loss parameters are therefore needed to be defined. Firstly, the value of the viscous and inertial resistance had to be formulated. For porous flow calculations, the viscous and inertial resistance, the first and second term on the right hand side respectively, can be seen in Forcheimer's equation which is

$$\frac{\Delta P}{L} = \frac{\mu}{K} v_s + C \rho v_s^2 \tag{3.4}$$

in which $\frac{\Delta P}{L}$, μ,K,C,v_s and ρ and is the pressure drop per unit length, dynamic viscosity, permeability, inertial flow coefficient, fluid density and the superficial velocity respectively. Permeability is a measure of the ease the fluid can pass through the solid and is linked to the effective surface length of the porous matrix[38][56] and has units meter squared. Inverse permeability, K^{-1}, is also termed viscous resistance[6]. The inertial flow coefficient can be determined from empirical correlations[6]. The superficial velocity is the net velocity through a cross sectional area for a given volume flow[56]. Forcheimer's equation is used in the Fluent software as a momentum sink (negative source) in the Navier-Stokes equation. The first term on the right hand side is commonly know as Darcy's law, which relates the volume flow in a porous medium to the pressure difference, analogous to Fourier's

law of heat conduction. Eq. (3.4) states that the pressure loss in a porous medium are defined by the sum two terms in which one is linearly proportional with the superficial velocity and the other is proportional with the superficial velocity squared. The significance of this relationship is that for flow with very low velocities (Reynolds number < 10), the pressure loss is considered to be linearly dependent on the velocity. While for higher velocities the inertial effect become more significant. After running a number of numerical tests to see the significance of the inertial loss term, it was observed that the inertial kinetics was negligible and using solely Darcy's law to formulate pressure loss is sufficient.

The permeability, K, seen in Eq. (3.4) was obtained after an evaluation of empirical correlations and experimental studies. From the empirical correlations, the packed bed and the specific surface approaches were used. The rationale of the packed bed method is to best estimate the wood chips as spherical bed particles. The packed bed method is best described via Ergun's equation[6][1]:

$$\frac{\Delta P}{L} = \frac{150\mu}{D_p^2}\frac{(1-\gamma)^2}{\gamma^3}v_s + \frac{1.75\rho}{D_p}\frac{(1-\gamma)}{\gamma^3}v_s^2 \tag{3.5}$$

in which D_p is the particle diameter, i.e. sphere diameter. Eq. (3.5) is a special case of Forcheimer's equation in which the packed beds has been included in the pressure loss calculation. Thus, only the first term was used. The two terms of Ergun's equation is originally two separate correlations that was merged by simply adding them together, they are known as the Blake-Kozeny and Burker-Plummer equations[1]. Therefore by omitting the second term on the right hand side of Eq. (3.5), one is left with the Blake-Kozeny equation and by rearranging the expression in terms of the viscous resistance, i.e. inverse permeability, the following expression becomes:

$$K^{-1} = \frac{150}{D_p^2}\frac{(1-\gamma)^2}{\gamma^3} \tag{3.6}$$

The particle diameter, D_p, needs further study in order to be determined. The unknown variable was determined by first measuring the wood chips from the lab. A representative sample of 30 wood chips were measured in thickness, length and width with a ruler. A graphical presentation of the measurements is displayed in Fig. 3.8. The measurements can be seen in appendix C.

Mean thickness, length and width were measure to be 0.4733, 3.77671, and 1.7700 respectively. The said measurements were used to create a representative cuboid, from which an equivalent diameter, d_{eq} of a sphere with the same volume-to surface-ratio to the wood particle was created. This method, known as the Sauter Mean Diameter(SMD) [62][73][2], can be calculated as

$$d_{eq} = \frac{6V_p}{S_p} \tag{3.7}$$

in which V_p,S_p is the volume and the surface area of the wood particle. A version of Eq. (3.6) that take the sphericity into account is also practised[62]. Sphericity equal to 1 is a perfectly spherical shape, while a lower number denotes less spherical. Less spherical shapes increases pressure loss as can be seen from the following equation

$$K = \frac{D_{eq}^2\Psi^2}{150}\frac{\gamma^3}{(1-\gamma)^2} \tag{3.8}$$

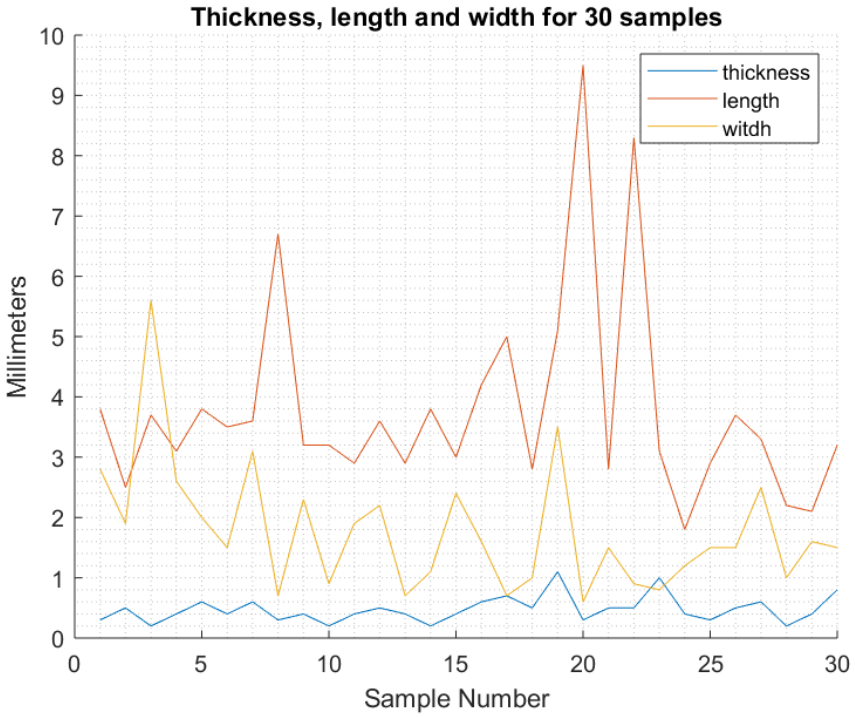

Figure 3.8: Measurements of wood particle

in which the sphericity can be calculated as

$$\Psi = \frac{\pi^{1/3}(6V_p)^{2/3}}{S_p} \tag{3.9}$$

However, these equations are highly empirical and should be used to expect a closer approximation rather than the correct answer. The outcome of the method described resulted in a equivalent diameter of 10.14 mm and a permeability of $6.556e-07m^2$. These valued were compared to values obtained in Mayherhofer et al. and Pozzobon et al.'s work[56][62]. From the work of the former, the samples of wood chips were sorted after small, medium and large sizes. From the large pile, an equivalent diameter of $8.7mm$ was achieved, with a maximum permeability of $26.4e-08[m^2]$ determined from pressure drop experiments through a $0.4m$ long cylindrical tube. Regarding the latter, an equivalent diameter of $3mm$ was measured from 536 samples, resulting in a lower permeability of approximately $1.70e-08m^2$ from a pressure drop across an $5m$ tube. By evaluating results retrieved from literature, the values obtained from the method described seemed satisfactory.

The last property of the wood material that needs to be discussed is the specific area of the wood chips. Specific surface area is the interface area between the pore volume and the solid matrix. It can be either defined as surface area per unit pore volume or surface area per unit mass of solid[76]. Specific surface area consists of the outer surface area as well as the inner surface area, as the gas may pass through the solid wood or char. The outer layer area was found by following a methodological

approach to determine the specific surface area per unit mass as described in the works Lunguleasa et al. [54]. The methodological approach by Lunguleasa et al. is a method of work which was used to calculate the quantity of the adhesive sprayed on the chip's surface area. It involves a virtual body of mass with a predefined base area cut into a desired number of layers, and by adding the surface areas of each layer the surface area per unit mass is determined. A demonstrative sketch can be viewed in Fig. 3.9.

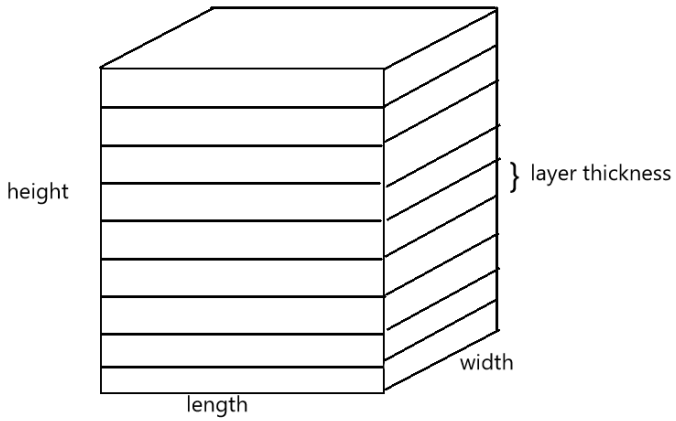

Figure 3.9: Sketch of the surface area calculation method

As for this case, the method goes as following: the density of wood used in this theses is 470 kg/m^3. A 100g block would make solid a volume of 212.77cm^3. Arbitrary base dimensions of 3x3cm would then result in a height of 23.64 cm. Layer thickness was selected to be 0.6cm based on an average of 30 measurements. As a result, 39.4 layers were created. The total layer surface area is therefore the product of number of layers, base dimensions and a factor 2 to account for each side. Thus, the total layer area of 709.2$cm^2/100g$ wood was achieved. The great advantage of this method is that it is possible to change the base area, yet total layer area would be the same. Moreover, the physical wood chips that this simulation attempts to describe numerically are ground to approximately the same layer thickness, but the length and with may vary greatly. The total layer surface area is the theoretical minimum surface area for two reasons: surface roughness is not taken into account and the edge sides of each layer is not included in the calculation. Although the surface area of wood chips might increase considerably when surface roughness is taken into account, surface roughness was omitted to facilitate the area calculation. As for the edge sides, a caution was detected as the total specific area (total layer area plus total edge sides) is now dependent on the former arbitrary base dimensions. 3x3cm base dimensions result in a total side edge of 283.7cm^2, while for example 5x5cm yields 170cm^2, all else given. A figure that describes the relationship between base dimensions and surface area is enclosed in Appendix C. It is therefore important to select dimensions that is approximated to that of the wood chips'. Using the average length units that was previously mentioned, a specific surface area of the outer layer was calculated to be 0.001258m^2/g, resulting in 1.0001 m^2 in aggregate for a 795g amount of wood chips. A

literature review was used to determined the inner surface area. Spruce properties were reviewed pine due to availability. In a doctoral thesis by Grønli it is stated that untreated spruce contain $0.19m^2$[40], totalling in $150.5m^2$ for all the wood chips combined. Conclusively, the method describe in Lunguleasa's paper would be a good method to estimate surface area, however the area covering the inner solid on a microscopic scale is much larger. The huge difference resulted in that only $0.19m^2/g$ will be used to define the specific surface. Spruce derived charcoal is in the same paper reported to contain 459 m^2/g. The area thus increases as the wood is in the converting process, but the scope of this thesis will only cover a constant value. The wood material properties can be summarized in Table 3.3, two of which will be used explicitly to define the porous region: inverse permeability and specific area.

Table 3.3: Wood particle properties

Name	Parameter	Value
Particle volume $[m^3]$	V_p	$3.145e-06$
Particle surface $[m^2]$	S_p	$1.860e-03$
Equivalent diameter $[m]$	d_{eq}	$1.014e-02$
Sphericity	Ψ	0.558
Permeability $[m^2]$	K	$6.556e-07$
Specific surface $[m^2/g]$	S_s	0.19

3.5.3 Gas properties

The gases used in the modeling were chosen to be CO, CO_2 and N_2, in which the volatile gases was a 50/50 mix consisting CO and CO_2 to facilitate the simulation work. These gases were chosen as they make up most of the volatile gases. Including more gases such as H_2 and CH_4 would have complicated the work needed to specify the temperature dependency of the mass sources and was for that reason not included. Nitrogen is used as a purge gas for case 4, and a standard gas to get started with the simulations for the first two cases. The gas density is temperature dependent expressed through the ideal gas law. The incompressible ideal gas was used, i.e. compressible flow are not considered to be relevant in the simulations. A constant specific heat capacity, thermal conductivity and viscosity were used for CO, CO_2 and N_2. CO and CO_2 share the same specific heat capacity equal to the mean value of their respective specific heats at 250^oC, due to the energy source balance that will be discussed later. Table 3.4 lists the values used for the gas properties.

Lastly, the final thermal property needed to be addressed was the convection heat transfer coefficient. The heat transfer coefficient was calculated in a similar procedure as described in Kurz et al.'s work[51]. The method was used to estimate the heat transfer coefficient of the heat exchange between a combusting wood particle and the gas for a fixed bed. The convective heat transfer coefficient was first obtained by estimating the Nusselt number, followed by the heat transfer coefficient calculation according to the following expressions

Table 3.4: Gas properties

Variable	Value
Density $[kg/m^3]$	
N_2	Incompressible ideal gas law
CO_2	Incompressible ideal gas law
CO	Incompressible ideal gas law
Thermal conductivity $[W/mK]$	
N_2	0.0410
CO_2	0.0362
CO	0.0414
Dynamic viscosity $[Pa \cdot s]$	
N_2	$2.685e-5$
CO_2	$2.456e-5$
CO	$2.748e-5$
Specific heat capacity $[kJ/kgK]$	
N_2	1062.0
CO_2	1053.0
CO	1053.0

$$Nu = \frac{h \cdot d_p}{k} = 2.0 + 1.1 \cdot Pr^{1/3} \cdot Re_p^{0.6} \tag{3.10}$$

in which, h,k, Pr and Re_p represent the convective heat transfer coefficient, thermal conductivity of the fluid, Prandtl number and the Reynolds number. Particle diameter, d_p, is as mentioned earlier the equivalent diameter, d_{eq}. Prandtl number was taken from 250^oC nitrogen gas. The Reynolds number is obtained by

$$Re_p = \frac{d_p|\vec{u_g} - \vec{u_p}|\rho_g}{\mu_g} \tag{3.11}$$

in which $\vec{u_g} - \vec{u_p}$,μ_g is the relative velocity of the gas tho the bed particle and the dynamic viscosity of the gas. The gas properties was nitrogen evaluated at 250^oC as well. The particle velocity was assumed to be stationary, and thereby considered to be 0. Based on trial simulations, an estimation of the flow velocity had to be made to arrive to a heat transfer coefficient. A summary of the values used can be seen in Table 3.5.

As the table shows, the resulting heat transfer coefficient was calculated to be 11.6 W/mK. The value is in good agreement with the empirical formula used in Lam et al.'s work [53]. Their correlation, expressed in degrees Kelvin, suggests $h = 5.69 + 0.0098T$ as a suiting formula for a pyrolysis process reaching temperatures of 800^oC. The use of this formula would have calculated a maximum heat transfer coefficient of $h = 13.26W/m^2K$ if a temperature of 500^oC was to be used.

Table 3.5: Convective heat transfer parameters

Name	Parameter	Value
Particle diameter $[m]$	d_{eq}	$1.014e-2$
Gas velocity $[m/s]$	$\vec{u_g}$	0.035
Gas density $[kg/m^3]$	ρ_g	0.609
Dynamic viscosity $[Pa \cdot s]$	μ_g	$2.685e-5$
Prandtl number	Pr	0.702
Reynolds number	Re_p	0.805
Heat transfer coefficient $[W/m^2K]$	h	11.6

3.6 Flow, Cell Zone and Boundary Conditions

This chapter describes how the numerical exercises were set up. The entries that apply to all the cases will be discussed at first, thereafter the adjustments for each case. The flow conditions for all cases include transient and laminar flow. In order to study the heating process and how the changing boundary conditions varies through time, one must include transient flow to accommodate the changes. The flow was selected to be modelled as a laminar flow regime. The reason behind this choice was due to the flow satisfying the laminar criteria $Re < 2300$ for internal flow. The energy equation needed to be included to account for temperature boundary conditions, conductive and convective heat transfer. Radiation modelling, however, was not included as solid conduction and solid-fluid convection will dominate the heat transfer. The flow was chosen to be a 2D-axisymmetric analysis. As previously mentioned, this was chosen to save the computational costs. This assumes the flow to be symmetric along the center line of the pipe furnace, i.e. no swirling effects. In order use axisymmetric flow, the symmetry line of the geometry needs to be aligned to the x-axis of the global coordinate system so that the axisymmetric flow equations can be used.

3.6.1 Flow equations

Mathematically, the software solves a set of partial differential equations (PDE) known as the governing equations of fluid flow. These include mass conservation, momentum equations and energy conservation. The PDEs are discretizised into algebraic equations onto which every set will be solved for each element, and collectively they describe the transportation of density, velocity, temperature and pressure. In addition, equations of state are necessary to formulate the thermodynamics of the fluid. The mathematical expressions depend on the nature of each problem, they also vary in appearance as the equation can be expressed mathematically in multiple ways. Here, the equations are acquired from ANSYS' Theory Guide[3]. Collectively for each case, the governing equations will include source terms that will be further discussed in the cell zone condition section. For an axisymmetric flow, the conservation of mass is expressed as

$$\frac{\partial \rho}{\partial t} + \frac{\partial}{\partial x}(\rho v_x) + \frac{\partial}{\partial r}(\rho v_r) + \frac{\rho v_r}{r} = S_m \tag{3.12}$$

in which v_x, v_r and S_m denotes the axial velocity, radial velocity and the mass source respectively. The mass source plays an important role in the following simulations as the volatile release is expressed in the source term of Eq. (3.12). The mass source will vary for each case and will be further discussed in the cell zone condition section.

The momentum equations are expressed through the Navier-Stokes equations for Newtonian fluids. As the flow analysis involved a 2D flow simulation, two transport equation were included, namely the axial and radial momentum. The axial momentum is given by

$$\begin{aligned}\frac{\partial}{\partial t}(\rho v_x) + \frac{1}{r}\frac{\partial}{\partial x}(r\rho v_x v_x) + \frac{1}{r}\frac{\partial}{\partial r}(r\rho v_r v_x) = -\frac{dp}{dx} + \frac{1}{r}\frac{\partial}{\partial x}\big[r\mu(2\frac{\partial v_x}{\partial x} - \frac{2}{3}(\nabla\cdot\vec{v}))\big] + \\ \frac{1}{r}\frac{\partial}{\partial r}\big[r\mu(\frac{\partial v_x}{\partial r} + \frac{\partial v_r}{\partial x})\big] + S_x\end{aligned} \tag{3.13}$$

in which S_x stands for the axial momentum source. The momentum sources in the x-direction include gravitational forces and a pressure loss force according to Darcy's law. The gravitational forces must be included to balance on the buoyancy forces that will occur due to density differences. The porous medium will cause a decrease the momentum throughout the porous domain. For this reason, the porous region is modeled as a momentum sink. The radial momentum equation equation is defined as

$$\begin{aligned}\frac{\partial}{\partial t}(\rho v_r) + \frac{1}{r}\frac{\partial}{\partial x}(r\rho v_x v_r) + \frac{1}{r}\frac{\partial}{\partial x}\frac{\partial}{\partial r}(r\rho v_r v_r) = -\frac{dp}{dr} + \frac{1}{r}\frac{\partial}{\partial x}\big[r\mu(\frac{\partial v_r}{\partial x} + \frac{\partial v_x}{\partial r})\big] + \\ \frac{1}{r}\frac{\partial}{\partial r}\big[r\mu 2(\frac{\partial v_r}{\partial r} - \frac{2}{3}(\nabla\vec{v}))\big] - 2\mu\frac{v_r}{r^2} + \frac{2\mu}{3r}(\nabla\vec{v}) + \rho + S_r\end{aligned} \tag{3.14}$$

in which the velocity vector, $\vec{v}$, is include the axial and radial velocity vectors and S_r is the radial momentum source. As discussed, the a negative momentum source will occur due to the porous medium. The momentum source was simplified to be of the same magnitude in both radial and axial directions.

The last flow equation is the energy equation. The energy equation handles the advective and diffusive heat transfer in fluid flow problems. The energy equation is the mathematical interpretation of the first law of thermodynamics for a given control volume. The energy equation is included as a part of the transport equations as heat transfer is a part of the simulations. When assigning a porous zone to a cell zone in ANSYS, the cell zone is by default modeled a fluid momentum sink. Consequently, the heat transfer originating from the boundary conditions will not take the solid wood properties in the calculations in the porous fluid region, except for an optional solid thermal conductivity. To overcome this, a "dual-cell" function was implemented. This functions creates a cell zone that directly coincides to the selected cell zone. Now, the there is one fluid cell zone dedicated to the desired gases overlapped by a solid cell zone that contains the wood properties. As a result, two energy equations are needed to describe the porous cell zone. The fluid and solid exchange heat through a source term present in both equations. For the fluid zone, the conservation of energy can be described as

$$\frac{\partial}{\partial t}(\gamma\rho_f E_t) + \nabla\cdot(\vec{v}(\rho_f E_f + p)) = \nabla\cdot(\gamma k_f \nabla T_f) + (\tau\cdot\vec{v})) + h_{fs}A_{fs}(T_s - T_f) + S_e \tag{3.15}$$

in which γ, E_f, τ and S_e denotes the porosity, total energy, viscous dissipation and energy source [4][7]. The energy source is related to the mass source described in Eq. (3.12). ANSYS models the mass source with a constant temperature of 25^oC. The mass source thus creates an unwanted energy sink when the domain increases in temperature. Therefore, the energy source is added to null out the energy sink. The details will be provided in the next section. The energy conservation for the solid region is given by

$$\frac{\partial}{\partial t}((1-\gamma)\rho_s E_s) + \nabla \cdot (\vec{v}(\rho_s E_s)) = \nabla \cdot ((1-\gamma)k_s \nabla T_s) + h_{fs} A_{fs}(T_s - T_f) \tag{3.16}$$

The two first cases, that do not involve a porous zone, use an energy balance equivalent to Eq. (3.15), without the heat exchanging terms, and a porosity equal to one.

An additional transport equation is included to accommodate for the species present in the simulations. The species transport equation is composed of the same terms as any transport equation: transient term, advective term, diffusive term and a source term. The transported quantity is local mass fraction, Y_i, of the individual quantity. The species are the aforementioned N_2,CO_2 and CO. For N number of species, $N-1$ species transport equations are needed to solve the quantity of species. The last species is solved by equating the difference of the former to species. The species transport equation is formulated as

$$\frac{\partial}{\partial t}(\rho_s Y_i) + \nabla \cdot (\rho \vec{v} Y_i) = -\nabla \cdot \vec{J} + R_i + S_i \tag{3.17}$$

in which J_i, R_i and S_i represent the mass diffusivity, production rate of species i due to chemical reactions and a species source[5]. The mass diffusivity is expressed through Fick's Law that formulates mass flux induced by difference in species concentration. R_i is considered to be zero as chemical reactions are not in the scope of this thesis. The species source term, S_i is the gas development that has been chosen to consist of $Y_{CO2} = 0.5$ and $Y_{CO} = 0.5$.

An assumption is made as the ideal gas law will be used for the state equation. This simplification is valid for certain gases if the pressure is sufficiently lower than critical pressure, and temperature significantly higher than critical temperature[**thermobok**]. The incompressible ideal gas law was used for the density formulation, which rules out compressible flow effects. For incompressible ideal gas, the density is formulated as

$$\rho = \frac{p_{op}}{(R/M_w)T} \tag{3.18}$$

in which p_{op},R and M_w is operating pressure (1 ATM), universal gas constant and molecular weight respectively.

The pressure and velocity was coupled through the PISO algorithm. PISO was developed for transient formulations[78] and has proven to ensure good stability for the four cases. Alternatively, the coupled scheme was considered as it is best suited for buoyancy effects, however for transient simulations considerably smaller time steps are required to reach stability. Second order upwind was selected for the momentum and energy equation rather than first order upwind to achieve a smaller numerical error.

The most suitable flow conditions, as discussed in the previous section, were determined through trial runs of the first case. The flow conditions are equal for each of the four cases. The cases differ

in the cell zone conditions as they approach a simulation that looks more and more like a pyrolysis process. The boundary conditions also differ in the last case, in which there is a gas inlet for the purge gas for the last case. As shown previously, Fig. 3.10 displays the faces and edges on which the cell zone and boundary conditions have been defined.

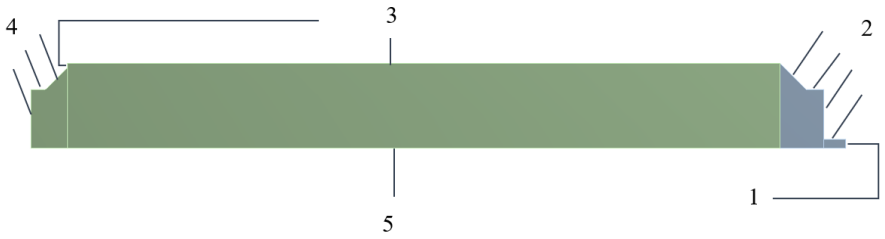

Figure 3.10: Fluid domain with marked faces and edges. Color and number indicate cell zone and boundary condition respectively

3.6.2 Case 1: uniform gas development

The first case aims to model a transient simulation with a uniform gas development. Nitrogen gas has been used, with properties described in Table 3.4. A constant mass source term was used to model the gas development. The mass source term is applied to the cell zone marked in green in Fig. 3.10 which contains the finite volume, V_2, resulting in a mass flow rate from the given cell zone. The mass source was modeled such that for a temperature of 500^oC, the volume flow at the outlet would be 3 L/min. This was achieved by mass continuity considerations. The mass source term was calculated from the two following equations

$$\dot{m}\left[\frac{kg}{s}\right] = S_m\left[\frac{kg}{s\ m^3}\right] \cdot V_2\left[m^3\right] \tag{3.19}$$

$$\dot{m}\left[\frac{kg}{s}\right] = \rho_{@500^oC}\left[\frac{kg}{m^3}\right] \cdot \dot{V}_2\left[\frac{m^3}{s}\right] \tag{3.20}$$

in which the conversion factor from m^3/s to L/min is 60e03. To satisfy a volume flow of $3L/min$ for the final temperature, the mass source term was thereby given the value 0.004178413 $kg/(s\ m^3)$. In addition to the constant mass source, an energy source had to be included to cancel the cooling effect the mass source had on the system. This was due to the software's built in settings that assigned a mass source temperature of 25^oC regardless of original cell zone temperature. Naturally, this caused an undesired heat sink that increased in significance the higher the surrounding temperature became. To overcome this problem, a User-Defined-Function (UDF) that specified a customized energy source was created. UDFs are programmable functions written in C/C++ that can be compiled or interpreted into the software. All UDF codes used in this thesis are attached in Appendix D. The UDF used executes an energy source term expressed as

$$S_e = S_m \cdot c_p\,(T - 298.15) \tag{3.21}$$

in which the energy source function presumes a constant specific heat. The temperature is the local temperature for a single element, or cell, expressed in Kelvin. In theory, the specific heat of an ideal gas should be a temperature dependent polynomial function. This requires Eq. (3.21) to be integrated together with the temperature difference term. The integration method was tried, with success, except for that the energy source never precisely matched the energy sink in magnitude due to a slight numerical difference. It was therefore decided to use constant specific heat where the cancellation did not pose any difficulties. The specific heat has for this reason chosen to be a constant value evaluated at $T = 250^oC$, as can be seen in Table 3.4.

The boundary conditions for the first and the next two cases are chosen to be pressure outlet, adiabatic walls and temperature boundary conditions. The said boundary conditions can be located through number 1, 2+4, 3 in Fig 3.10. The value of the pressure outlet is supposed to reflect the operating conditions, i.e. 101325 Pa. The outlet temperature is taken to be 20^oC, which is considered to be the room temperature. The top and bottom surfaces (2 and 4), an assumption have been made as the surfaces have been assigned an adiabatic boundary condition (heat flux = 0) which will not be true in a real case. The boundary condition assigned to the wall (3) is a transient temperature boundary condition. The temperature has a heating rate of $13^oC/min$, ranging from 20-500^oC. The heating process has been calculated to take 2220 seconds, or 37 minutes, which is the minimum flow time of the simulations. To formulate the transient boundary condition, a new UDF was created. The function returns a wall temperature, T_w, given by

$$T_w = 293.15 + 0.216216 \cdot t \tag{3.22}$$

in which t denotes the time in seconds. The starting time is $t = 0$, and minimum ending time is $t = 2220$. When the wall temperature reaches $773.15K$, i.e. 500^oC, the wall temperature will continue to stay this temperature. The script can be viewed in Appendix D. Prior to the transient simulations, the initial conditions of 20^oC temperature across the entire domain and and constant source terms were run for 200 iterations in steady state.

3.6.3 Case 2: uniform gas development in porous media

Case 2 incorporates a porous zone into case 1. This was done by assigning the desired zone a porous region. The porous zone was selected to be the green region viewed in Fig. 3.10, same region from which the mass source appears. Essentially, when assigning a porous region, a new term is added to the momentum equation. The term is the pressure loss equation that can be seen in Eq. (3.4). Hence, the input variables that need to be specified are the variables present in Forcheimer's equation. As previously mentioned, only the viscous term was used due to negligible kinetic motion. The permeability, was assumed to be isotropic, that is equal in both axial and radial direction. The input entry of the permeability is the viscous resistance. Therefore, from Table 3.3, the permeability was inverted and a value of 1526000 m^{-2} was achieved. Porosity of the wood chips was calculated to be 0.68, and was chosen to be constant as well.

Furthermore, the heat transfer settings had to be changed. The default setting assumed that the gas and solid was of the same temperature. The same setting considered the mass and fluid as one medium, in which the specific heat and density was that of the fluid, while the thermal conductivity

belonged to the solid wood defined in the materials section. A non-thermal equilibrium model was utilized in which a new solid cell zone was created. A new cell zone enabled a new energy transport equation which allowed the gas phase and solid to have different temperatures. Similar to the first case, the mass and energy source term have been used for the gas development. As seen in Eq. (3.15) and (3.16), the energy source term was deliberately chosen to appear in the fluid energy equation. This is due to the mass source originating in the fluid domain. A modeling limitation was noticed as ideally, the local mass source of the fluid for a given cell should be given the same temperature as the overlapping solid cell to imitate an evaporation process. This can possibly be solved through a new UDF, however the time was too limited for an attempt. Instead, the working model used used the fluid temperature to as mass source temperature.

The final specifications needed to complete the porous non-thermal equilibrium formulation was the interfacial area density and convective heat transfer coefficient. The interfacial area density is the name used to describe volume specific surface area $[1/m]$ such that for a given bulk volume, the interfacial area $[m^2]$ between solid and the pore volume is determined. From Table 3.3, the specific surface acquired from Grønli's doctoral thesis was said to be 0.19 g/m^2. The interfacial area density was then calculated from a solid mass of 795 g, and bulk volume of 5.283 L. As a result, the interfacial area density was determined to be 28598 $1/m$. The surface area between the solid and fluid is thus 151 m^2. The heat transfer coefficient was determined to be 11.6 W/m^2K as discussed in section 3.5.3. Nitrogen gas was also the only gas present in the simulation. The simulation was run in steady state with the initial values as boundary conditions, before the transient simulations began.

3.6.4 Case 3: Temperature dependent gas development in porous media

The third case is replaces the uniform gas development with a gas development as a function of temperature. The gas development continues to be represented by a mass source, though the source term is formulated by a new UDF. The goal of the function was to achieve a mass loss rate equal to that of biomass undergoing pyrolysis. Normally, what can be expected from pyrolysis experiments of woody biomass is to see almost no, or little, volatilization for temperatures outside the 220-400^oC range. As for mass loss rate inside the range, a bell shaped exponential curve is observed with a clear peak. The exact temperature range depends on the operating conditions, however in most cases they are expected to be observed between the 220-400^oC mark. The UDF was written to keep the mass source term as simple as possible. For a single cell, the source term was programmed to be either on or off by an if-statement. Over time, the cells in the porous media should collectively create a mass loss rate similar to the shape of a bell curve as more and more cells become activated during the heating process, followed by an increasing amount of cells becoming deactivated as the temperature exceeds the "on-criteria". Fig. 3.11 illustrates how each cell in the porous medium behaves for a given temperature.

The if-statement states that the mass source is equal to zero for all temperatures less than 223^oC and greater than 399^oC. The source term value of 0.081 $kg/s\ m^3$ was chosen after a number of tests. The value was chosen to satisfy a 75% mass loss during the flow time. The total mass loss was measured by integrating the mass flow rate with respect to time in MATLAB. In these

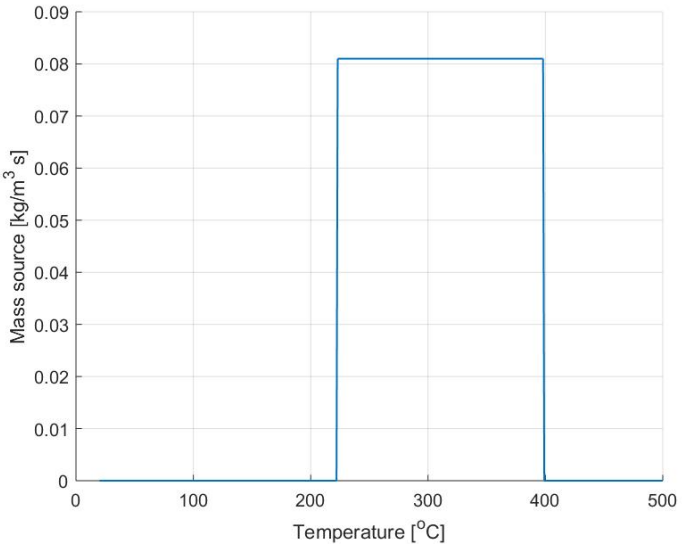

Figure 3.11: The temperatures for which the cells produces a mass source

simulations, the mass inside the computational domain do not change as the wood density is of a constant value. If the time would permit it, an attempt to write an UDF for the wood density as a function of the mass flow rate should have been done.

The species transport model was enabled to include CO and CO_2 as mass source terms. The mass sources were given a constant specific heat value for the same reason as with the nitrogen gas. Both a mass source UDF and an energy source UDF were written for this case. It was determined that CO and CO_2 have the same specific heat value so that only one UDF specifying energy source had to be written. The mass source was specified such that $S_m = 0.081$ and $S_{m,CO} = 0.0405$ for the said temperature range. Consequently, the CO/CO_2 ratio is equal to 1. Neither diffusion energy source nor any volumetric reaction rates were enabled, as more research is needed to comprehend the significance of such processes. The purpose of enabling species transport was to include the thermal properties of the gases in the simulation. The solution was initialized by running a steady state case of the initial conditions with a nitrogen mass fraction equal to 1 in the whole domain.

3.6.5 Case 4: Temperature dependent gas development in porous zone with purge gas

Case 4 explores the dynamics of the system by modifying the geometry with a gas inlet on the bottom. The gas will sweep over the pyrolyzing environment as a purge gas would in physical experiments. The inlet diameter is 0.48 inches, or roughly 12.2 millimeters, matching the size of outlet diameter. The mass and energy source are formulated through UDFs in the same way described for case 3. The gas inlet boundary condition was a constant 500 mL/min volume flow with a nitrogen gas of mass fraction equal to 1. As the inlet area was predetermined, a velocity inlet boundary condition

valued $v = 0.07138 m/s$ maintained the desired volume flow. Constant temperature of 20^oC was used for the velocity inlet throughout the simulation. The solution was also initialized with a steady state case of the initial conditions.

The cases are summarized in Table 3.6. The table describes the modifications compared to the Case 1, which serves as a base case. The dashed lines signify that the entry from the base case was kept.

Table 3.6: Case Matrix

	Case 1	Case 2	Case 3	Case 4
Flow	Transient Laminar 2D-Axisymmetric Heat Transfer	- - - -	- - - - Species Transport	- - - - Species Transport
Materials	N_2	-	- CO_2 CO	- CO_2 CO
Cell zone	S_m = constant S_e = constant	- - Porous medium	$S_m = S_m$(T) $S_e = S_e$(T, S_m) Porous medium	$S_m = S_m$(T) $S_e = S_e$(T, S_m) Porous medium
Boundary	Outlet: Temperature = 20^oC Outlet: Pressure = 101325 Pa Top, bottom: adiabatic walls Wall: $T_w = T_w(t)$	- - - -	- - - -	- - - - Inlet: Temperature = 20^oC Inlet: velocity = 0.07138 m/s
UDF	$T_w = T_w(t)$ $S_e = S_e(T)$	- -	- $S_m = S_m(T)$ $S_e = S_e(T, S_m)$	- $S_m = S_m(T)$ $S_e = S_e(T, S_m)$

3.6.6 Final steps

The final step of the methodology was to determine the size of the time step. The time step was decided to be self-determined in the end, with an intent to achieve a stable and a computational cost efficient solution. The same step size was used in all cases, with a value of $t = 0.1s$. For case 2, a step size using $t = 0.05s$ was experimented to detect any differences on the outlet temperature. The results showed a negligible difference, and thus a step size of 0.1s was selected. The most essential criteria for the time step is to satisfy the Courant–Friedrichs–Lewy (CFL) condition. The CFL condition states that the time step needs to resolve the convective motion of a fluid particle from one cell to the neighboring cell. It is expressed as

$$C = v\frac{\Delta t}{\Delta x} \tag{3.23}$$

in which C is the Courant number, v,Δt and Δx are the velocity, time step and element size respectively. Mathematically, it is required from Eq. (3.23) that $C \leq 1$ to ensure a non-diverging

solution. A check to verify the the CFL condition for the four case proved to be fairly good, as the velocity needed to be maximum $0.01m/s$ given the conditions of $\Delta t = 0.1s$ and $\Delta x = 0.001m$. This is mostly true for the first two cases, and in the porous medium for the latter two, however choosing a more refined time step size would be optimal, or increasing cell size if possible. Free convection will require smaller time steps that free convection in porous medium because of the velocity. To compare, relevant literature describing selecting the time step of natural convection has been reviewed. Sozio and Sapia developed a transient CFD model of natural convection of heat sink effects of fins[67]. The time step was reported to be $\Delta t = 0.001s$ for which the simulation took 13 days to finish. The chosen time step was also compared to ANSYS Fluent's guideline to determine the time step for transient natural convection[8]. It is given by

$$\tau = \frac{L}{U} \approx \frac{L}{\sqrt{g\beta\Delta T L}} \tag{3.24}$$

in which τ is the time constant, from which $\tau/4 = \Delta t$. Acceleration due to gravity and volumetric thermal expansion are denoted by g and β respectively. The length scale was the diameter of the cylinder, and a conservative estimation 480^oC temperature difference was used. The calculation suggested a time step size of $\Delta t = 0.029s$. Calculation input can be viewed in Appendix E. As a conclusion, the optimal size of time step should be lower although the some indications imply that the time step might suffice. Number of iterations per time step was decided after some trials to be 20.

Lastly, the simulations were decided to be run at NTNU's cloud computing cluster IDUN. To be run successfully, a batch file, case files, UDFs and a journal file had to be attached. The task of the batch file, which communicates in the cluster's Linux based language, is to start the Fluent's journal file. The journal is a text file containing Text-based User Interface (TUI) commands, instructing the UDFs to be compiled and the simulations to start. The calculation used about 4 hours to complete the heating process of 37 minutes, and about 13 hours for a maximum flow time of 100 minutes.

Chapter 4

Results and Discussion

The case number is the order of results‘ appearance. Each case will be presented with a particular focus area in mind. As for the first case, a calculation check to validate the results against theoretical values is done. Same goes for case 2, with regard to the porous medium. To describe the general behaviour of the system during the heating process is the task for case 3. And to see how a cold gas inlet inflicts case 3 was studied by case 4.

4.1 Case 1

Mass flow calculations were performed to investigate the continuity requirements. Table 4.1 displays the calculations performed for the last time step, as the steady state solution has at that point arrived. The table shows that the numerical calculations are in good agreement with the anticipated theoretical values. As previously mentioned, the mass flow rate is the product of source term and the cell zone volume, and following the volume flow can by obtained by dividing the mass flow rate by its density according to Eq. (3.19) and (3.20). The target of the first simulation case was to achieve a 3 L/min volume flow when the system reached 500 ^oC. As $4.956E-05 m^3/s$ is larger than a L/min volume flow by a factor of 60e+03, it can be observed that numerical computation reached a satisfying value. Outlet velocity and Reynolds number calculations demonstrate that the buoyancy flows suit a laminar flow model as far as this case is concerned. The difference of the predicted values relative to the results shows that the mass flow calculation for that particular time step is

Table 4.1: Mass continuity calculations

	Theoretical	Results	Difference
Mass flow rate $[kg/s]$	2.207500e-05	2.207502e-05	-0.00009060 %
Volume flow rate $[m^3/s]$	5.000e-05	4.956E-05	0.88 %
Velocity $[m/s]$	0.428	0.429	-0.20 %
Re	15.290	15.320	-0.20 %

very accurate. The volume flow calculation deviates the most. Mostly likely, it is attributed to the accuracy in the density hand calculation. It is nevertheless a very small deviation, and therefore considered a valid result. The numerical results prove to be coherent with the anticipated hand calculations and are thus taken to be very reliable.

The velocity profiles were investigated at three cross sections. They were selected to be evenly spaced across the straight pipe section, at: $x = 0.10m, x = 0.25m$ and $x = 0.40m$. At these locations, the velocity profiles were also investigated at 4 time steps: for t = 10, 20, 30 and 40 minutes. The velocity profiles were created with CFD-Post prior to further processing in MATLAB. They can be displayed in Fig. 4.1. Collectively, for the selected x-values it can be revealed that the highest velocities can be observed at around 10 min, possibly before, and onwards the axial velocity decreases in magnitude. In addition, the figures reveal that the gas close to the reactor walls travels in positive x-direction, while the gas closer to the center travels towards the bottom. This is most likely attributed to that the heat transfer from the walls induce the motion of the gas due to buoyancy effects. Evidently, Fig. 4.1 suggests that some the gas participates in a circular motion in which the gas moves upwards along the walls, meet in the middle and travel downwards along the center. The point at which the axial velocity is neither positive nor negative seems to occur on two occasions for each time step. As the motion of the fluid travels in large circles, the point at which the velocity profile is zero should be the center point of the rotating fluid. A guess will be that the center point is taken to be point at which the fluid particle rotates about its own axis. The physics of rotating fluid particles is nonetheless not included in the simulation software and therefore it cannot be observed visually. However, as this model presumes a laminar flow model, the particle paths of the fluid are forced to travel without interference of neighboring particles and might possible give a wrong image of the flow characteristics. Further studies are needed to conclude whether or not a laminar model appropriately describe the fluid dynamics in this case. Fig. 4.1 describe a decreasing magnitude of the velocity in both directions. As time progresses, the heat transfer from the wall will decrease as the system and wall temperature difference decreases. As a result, the effect of the induced buoyancy flow reduces, decreasing the gas velocities. For a steady state solution in which the whole computational domain is in thermal equilibrium, a velocity profile equal to that of a hydrodynamic fully developed flow is expected to be seen. However, what Fig. 4.1 describes is that there is a small temperature difference between the wall and the gas. Therefore, it is implied that the system is not in thermal equilibrium, which can be explained it being due the steady state solution involving the uniform gas source to leave the reactor before reaching 500^oC.

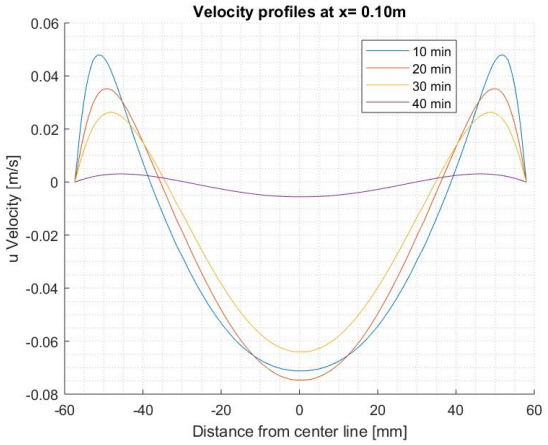

(a)

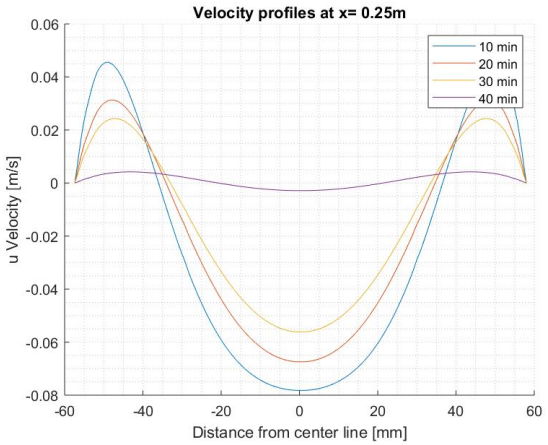

(b)

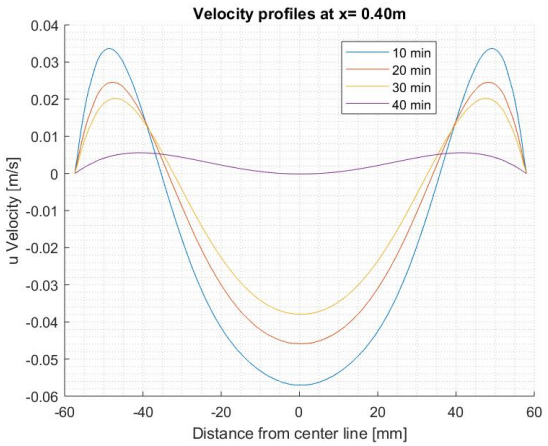

(c)

Figure 4.1: (a) Transient velocity profiles at (a) x = 0.10m (b) x = 0.25m (c) x = 0.40m

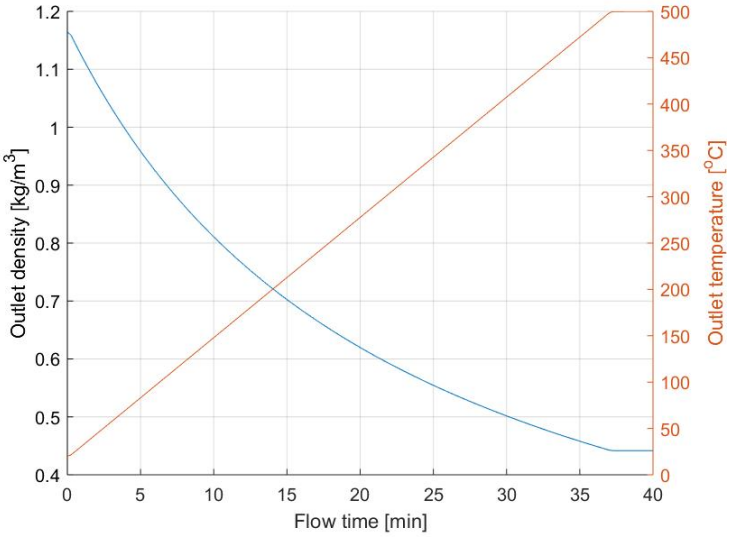

Figure 4.2: Temperature and density of the outlet

The temperature of the outlet gas and its density can be viewed in Fig. 4.2. The outlet properties demonstrate the density's dependency of temperature quite well. As discussed in section 3.5.3, the density of the gas is defined by the ideal gas law. The relation between the density and the temperature can be describes as $\rho \propto 1/T$. As shown in Fig. 4.2 the inverse proportional relationship of between the density and temperature of the gas is well described. Measurements of the gas at the outlet show a 499.84^oC temperature in the end of the simulation. This can either be true or a close approximation, or attributed to a significant numerical error. Further study needs to address this question, it be testing a new numerical scheme or to refine the time discretization. The time at which the outlet temperature flattens is fairly close the 37 minutes mark, which is the time the wall temperature reaches 500^oC. The gas at the outlet reaches constant value of 499.84^oC approximately 135s after the wall reaches constant temperature.

4.2 Case 2

Table 4.2: Mass flow, volume flow and pressure loss calculations

	Results	Difference
Mass flow rate $[kg/s]$	2.209775e-05	-0.10305323 %
Volume flow rate $[m^3/s]$	4.949e-05	1.02 %
Pressure loss $[Pa]$	0.177	-292%

Mass and volume flow calculations still proves to be satisfactory for the last steady state calculation. It can be seen that the porous medium has a moderate impact on the mass flow rate. In theory, for a steady state case the mass flow rate should be constant, although the fluid experiences a sink. Thus, in case 2, the porous medium contributes to a slight error in the continuity balance. Pressure loss across the fluid domain was also measured. With a value of 0.18 Pa, the calculations show that the pressure loss is almost absent. A pressure drop close to zero is in this case most likely caused by two factors: one being that the fluid velocity is very low, the second being the length of the reactor. The average velocity in the axial direction was calculated to be 0.004 m/s at the end time of $t = 40min$. From Ergun's equation of pressure loss in packed beds, formulated in Eq. (3.5), the estimated pressure drop would be approximately 0.05 Pa. The empirical value differs greatly from the numerical one. The reason behind this might be that there are many more variables in play in the simulation, such as heat transfer, thermal properties of the fluid, numerical limitations etc. A negligible pressure drop is however considered credible as similar experiments point to the same. In Fig. 4.3, results obtained by Mayerhofer et. al is displayed. In their work, the pressure drop of wood chips with equivalent diameters of 3.4-8.7mm was studied experimentally. Each curve in the figure represents the pressure loss per unit length for a particular size category. What can be observed is that the largest particles, due to its greater permeability, have the least pressure drop and vice versa. With reference to this case, a velocity of 0.004 m/s and particle size proximate to 10.14mm will therefore be very close to zero.

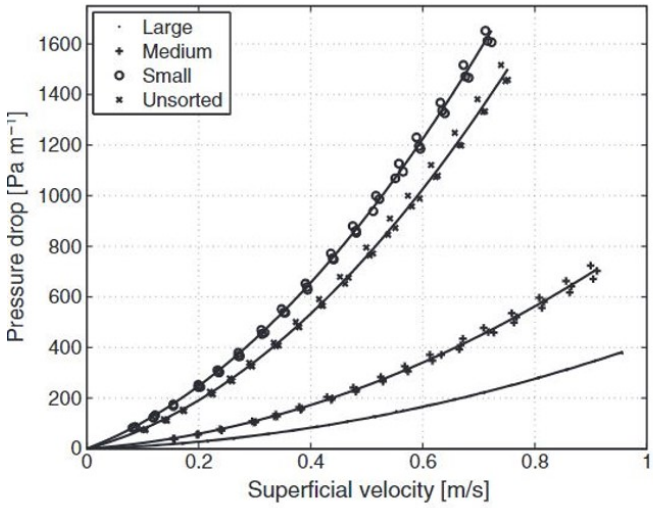

Figure 4.3: Pressure loss curves derived from experiments of wood chips. Source: Mayerhofer et al.[56]

The gas and wood materials were separated by assigning them a cell zone each. The purpose was to model a heat transfer mechanism between the gas and the solid phase. The phases communicate through a source term embedded in each of the energy equations, as shown in Eq.s (3.15) and Eq.s (3.16). From Fig. 4.4, it can be seen that the source term is equal to zero. The figure implies that the phases are in thermal equilibrium - that no heat is transferred from one phase to another. The implications Fig. 4.4 have on the simulation is either that a non-thermal equilibrium model is not necessary for the current case, or that the figure is not correct. The velocities inside the porous domain is in the order of 10^{-3}, therefore there is it is possible that the fluid spend enough time in the porous domain so that the gas and fluid reach thermal equilibrium. Additionally, the heat transfer area between the phases is very large resulting in a very effective heat transfer. On the other hand, the gas and wood increase in temperature at completely at difference rates, as the mass and specific heat capacity is in order of 1000 times larger in wood compared to the gas.

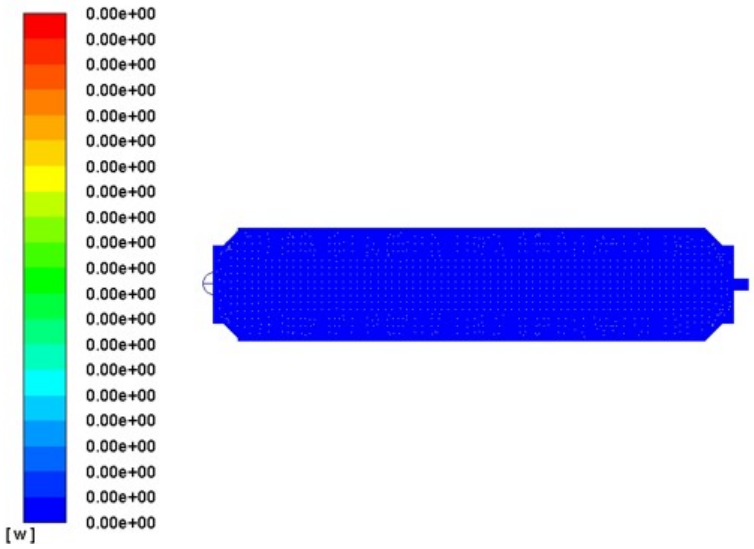

Figure 4.4: Non-equilibrium thermal source

4.3 Case 3

Regarding case 3, the goal of the mass flow rate was to arrive to a temperature dependent mass source. The mass source function was programmed so that a total mass loss would be equivalent to 75% of initial mass. The results of the mass flow rate at the outlet is displayed in Fig. 4.5. The mass flow rate curve of Fig. 4.5 (a) was integrated numerically in MATLAB, using a function employing the trapezoidal numerical integration method. The aggregate mass that had passed the outlet was estimated to be $0.584kg$. The supposed mass loss is therefore 73.4% of the $0.795kg$ starting point. 73.4% is considered a very good approximation, and by studying the shape of the curve, it can be determined that the mass flow rate approximation is satisfactory compared to relevant literature. The abrupt start of the curve followed by a peak and ending with a more moderate decrease is a typical biomass pyrolysis DTG curve. Some qualities are nonetheless necessary to improve. Firstly, the peak is not as defined as physical experiments suggest. The curve of the mass flow rate with respect to time is compared to Wang et al.'s work of pine wood pyrolysis as the operating conditions are quite the same: $100mm$ diameter and $800mm$ reactor length of electrically heated pinewood in a $9.2^oC/min$ heating rate. Their results can be viewed in Fig. 4.6. The peak observed is clearly defined right after a steep increase, followed by a more moderate decrease. Additional peaks are also observed, originating from cellulose and lignin decomposition, which the numerical model lacks.

A faulty weakness of the simple mass source function can be detected around the 16 min mark of Fig. 4.5. This slightly discontinuous bend is a result of mass source of the porous medium directly bordering the wall going from 0 to $0.081kg/s\ m^3$ in an instant when the wall temperature reaches 496K, or 222^oC. This will according to the wall temperature function described in Eq. (3.22) happen after 15 minutes and 40 seconds. The function is therefore deemed rather unphysical, as the volatilization of biomass appears more gradually. Additionally, the "on-and-off" function of the

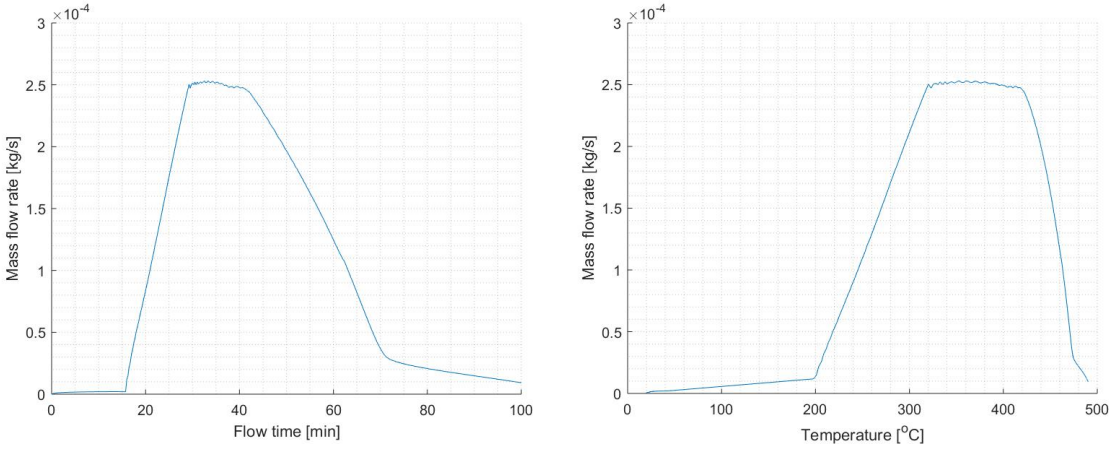

(a) (b)

Figure 4.5: Mass flow at the outlet displaying: (a) mass versus flow time (b) mass versus outlet temperature

mass source is discontinuous itself which can lead to stability issues. To improve on this, the function should be replaced with a differentiable and continuous curve such as a sine curve.

As the source term function is not activated until roughly 16 minutes, the small amount of mass flow that can be observed in the first minutes should be the initial gas occupying the reactor space expanding and partly leaving the reactor. The last minutes show that the solution has not reached a constant mass flow rate, i.e. a steady state solution is not obtained after 100 minutes.

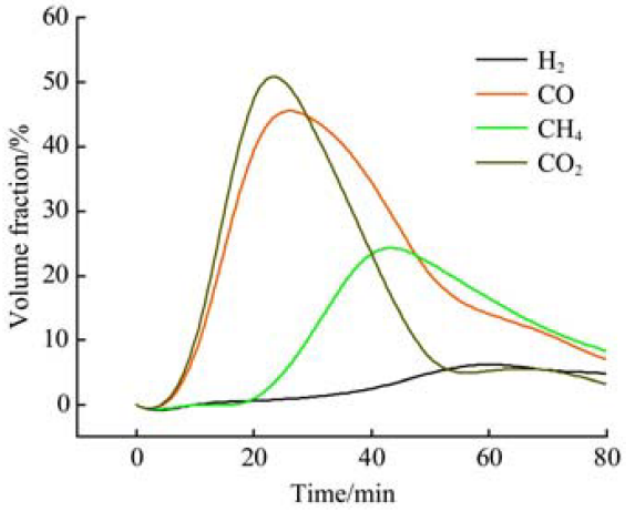

Figure 4.6: Gas development of pine wood pyrolysis. Source: Wang et al.[79]

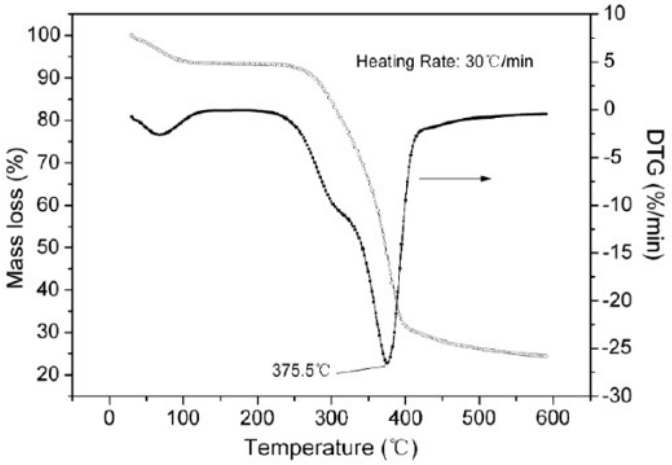

Fig. 3. TG and DTG curves for pine wood at a heating rate of 30 °C/min.

Figure 4.7: TG and DTG curves of biomass pyrolysis. Source: Bosong et al. [52]

The outlet mass flow rate was plotted against the outlet temperature to determine at which temperatures the mass flow rate is the highest, and to see how accurate the results are when compared to literature. The results can be seen in Fig. 4.5 (b). Similar to Fig. 4.5 (a), the peak is flat for an extended temperature range and can be seen with small fluctuations. The fluctuations over the extended period of time is assumed to be caused by a shift, from an overweight of mass sources being active to the opposite. The wide temperature range, which is approximately considered to be from 200 ^oC to 490^oC, could be caused by a wide active mass source criterion from the UDF. By reprogramming the mass source function in favor of a narrower range, it is believed that a more accurate bell-shape curve is obtained. The reprogramming should also include a more continuous curve, as discussed, to avoid the issue with a sudden mass source appearing in an instant, which will be more prevalent for a narrower criterion. Fig. 4.5 (b) was compared to the work of Bosong et al.[52], whose experiment reads a temperature range from 200-400^oC. The temperature range is quite typical for conventional pyrolysis and should therefore be a quite valid reference frame for Fig. 4.5 (b). Evidently, the results from the simulations produced a too wide range. It is observed that if the "plateau" were to be replaced with a defined peak, the resulting range would be quite satisfying.

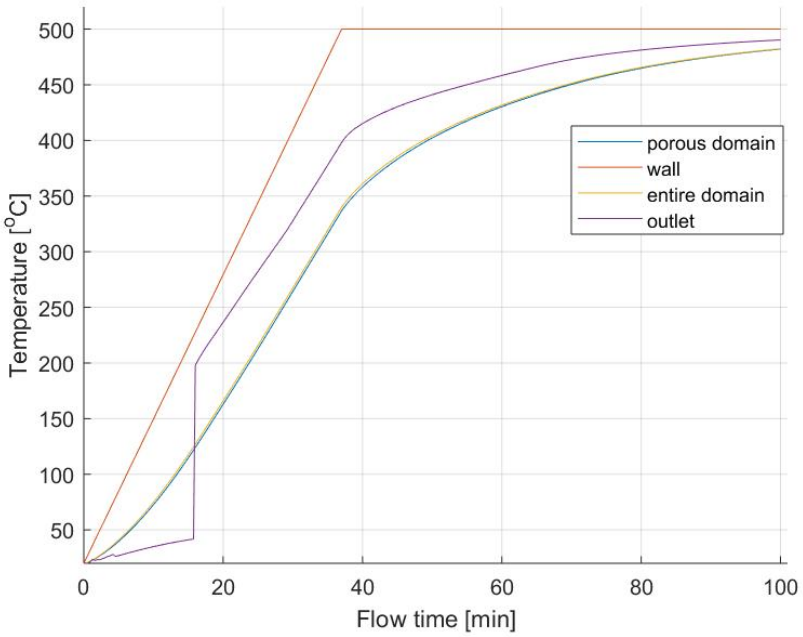

Figure 4.8: Temperature curves of selected locations with respect to time

Comparisons of temperatures with versus time of selected locations can be viewed in Fig. 4.12. The curve with the label "entire domain" denotes all faces and edges that make up the entire reactor. Furthermore, the "porous domain" label denotes the area weighted average of both the solid and fluid cell zone that make up the porous domain. As discovered earlier, they are taken to be of the exact same temperature, so only one cell zone would in practice suffice. It is also observed that there is almost no difference between the porous domain and the entire domain. That is plausible since the porous domain cover the vast majority of the control volume. Thermal inertia is observed as the porous domain is seen to be heated with time lag of approximately 10-20 minutes the first half of the flow time. During the second half of the flow time, the measured temperatures start to form an asymptotic pattern relative to the wall temperature. Seemingly, as the fluid temperature approaches the wall temperature, the slope of the temperature curve decreases which ultimately slows down the heating process. Ideally, longer runs should be the carried out to decide the time it will take the system to reach steady state, however the calculations are limited by the computational cost and the computer memory. Alternatively, it can be reasoned that a steady state solution can be reached earlier if the wood density would decrease as it should.

An energy conservation calculation was carried out to asses the rate at which the system is heated. The calculation should also indicate whether or not the system reaches a steady state solution. In Fig. 4.12, the heat transfers due to wall boundary conditions, mass flow at the outlet and the mass source are added together. The results show that the heating rate of the system with respect to time is the highest during the first half of the process, with a peak value right before 40 minutes.

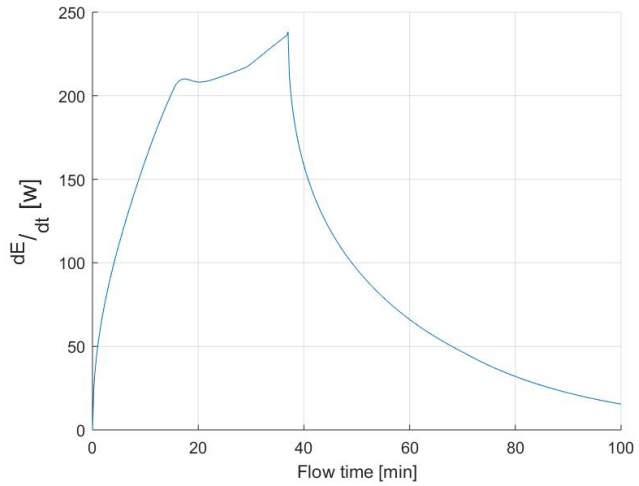

Figure 4.9: Transient energy balance: sum of wall heat transfer, outlet heat transfer and mass source energy generation

The peak value signifies when the heating rate of the system is the highest, and it is expected to be very close to when wall temperature reaches constant. This is because as time progresses, it can be seen that the gap in temperature between the wall temperature and the domain keeps increasing until the wall reaches 500^oC. After this point, the gap begins to close. For a steady state solution, the energy balance should be equal to 0, which Fig. 4.12 indicates that the system is gradually in the process of. The shape of the curve looks somewhat unnatural. Here, it is reasonable to believe that a numerical error is present as values, particularly at the curve peak, is seen to change very quickly. The curve suggests that some improvement is needed to achieve a more refined curve.

4.4 Case 4

To study the impact the purge gas has on case 3, the mass flow rates have been plotted in Fig. 4.10. The clearest difference can be observed after approximately 70 minutes. As the mass flow rate of case 3 continues to decrease towards the outlet conditions observed initially, the mass flow in case 4 is seen to be rather constant, and also significantly higher than the initial conditions. The figure implies that the mass source function in some domain regions continues to be activated. This is most likely caused by the cold inlet gas of 20^oC that keeps the lower area of the reactor to produce a costant mass source. To improve on this, the mass source should be limited by the existing density of the solid wood so that a more correct mass loss is achieved. The initial constant mass flow rate seems to be accurate, as the product of the density, velocity and the inlet area were anticipated to be $9.67e-06\ m/s$.

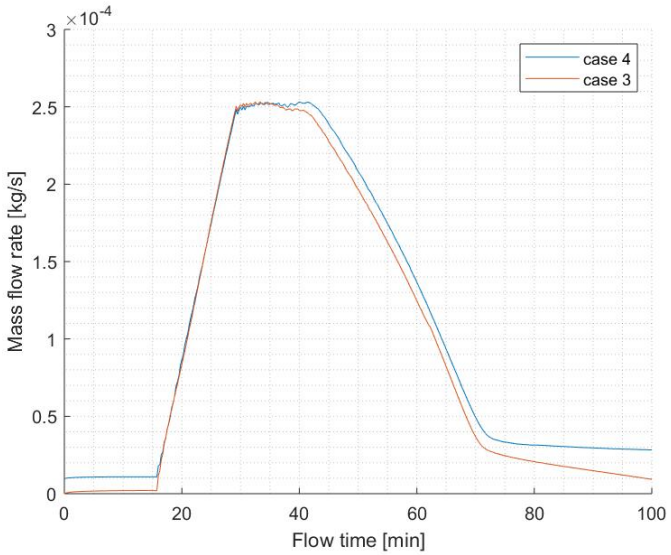

Figure 4.10: Case 3 and 4: Mass flow rate with respect to flow time

A new look on the temperature curves describing the average domain temperature has been made. The results can be seen in Fig. 4.12. The rate at which the case 4 domain is heated is similar to that of case 3, which is can be interpreted that the cold inlet gas has almost no impact on the global temperature. The temperature curve is shown to be slightly less in case 4, which can be explained by the heating of the nitrogen slows down the heating process.

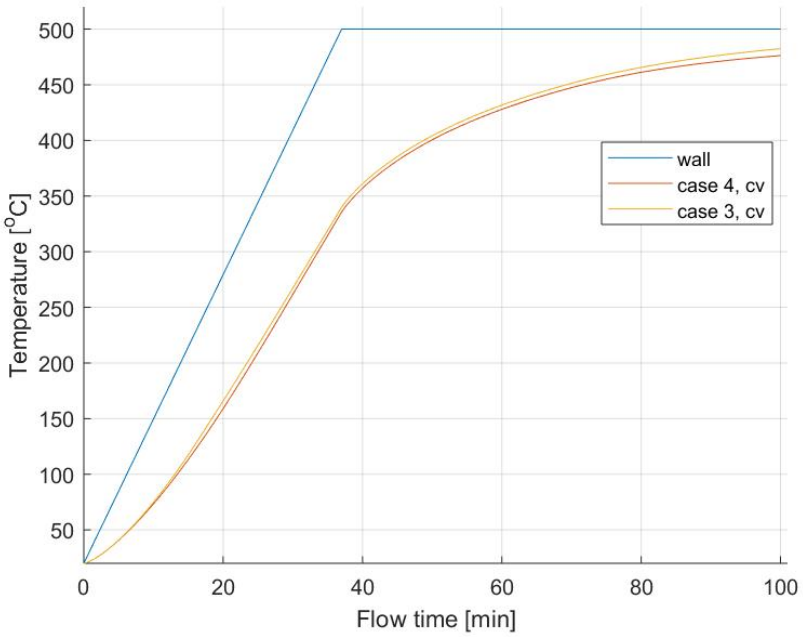

Figure 4.11: Temperature curves of case 3 and case 4

Contour plots of the reactor in case 4 is shown in Fig. 4.12 for three different flow times: 37, 70 and 100 minutes. Regarding the former, the contour plot displays the temperature distribution of the reactor when the wall temperature turns constant. The bottom section is seen to be approximately 110^oC and less which is quite cold relative to the rest of the domain which is taken to be approximately 340^oC. The temperature difference between the bottom section and the rest of the domain has neatly created a dividing line at the interface. The defined temperature separation might possibly be due to the position of the wall boundary conditions. The direction most of the fluid travels is in this case strongly influenced by the gas inlet. As conduction and convection are the only heat transfer modes enabled in this simulation, the heat from the wall will most efficiently travel in the fluid direction resulting in higher temperature observed on the top. The conduction will mostly be responsible for the heat transfer in the radial direction, as well as the negative axial direction. Therefore, the point at which the temperature boundary conditions end will create an interface where the temperature is relatively low in the radial direction and significantly lower below its x-position. As time progresses, the temperature of the bottom is slowly heated, gradually narrowing the cold temperature distribution. Furthermore, the rest of the domain approaches a more uniform temperature distribution.

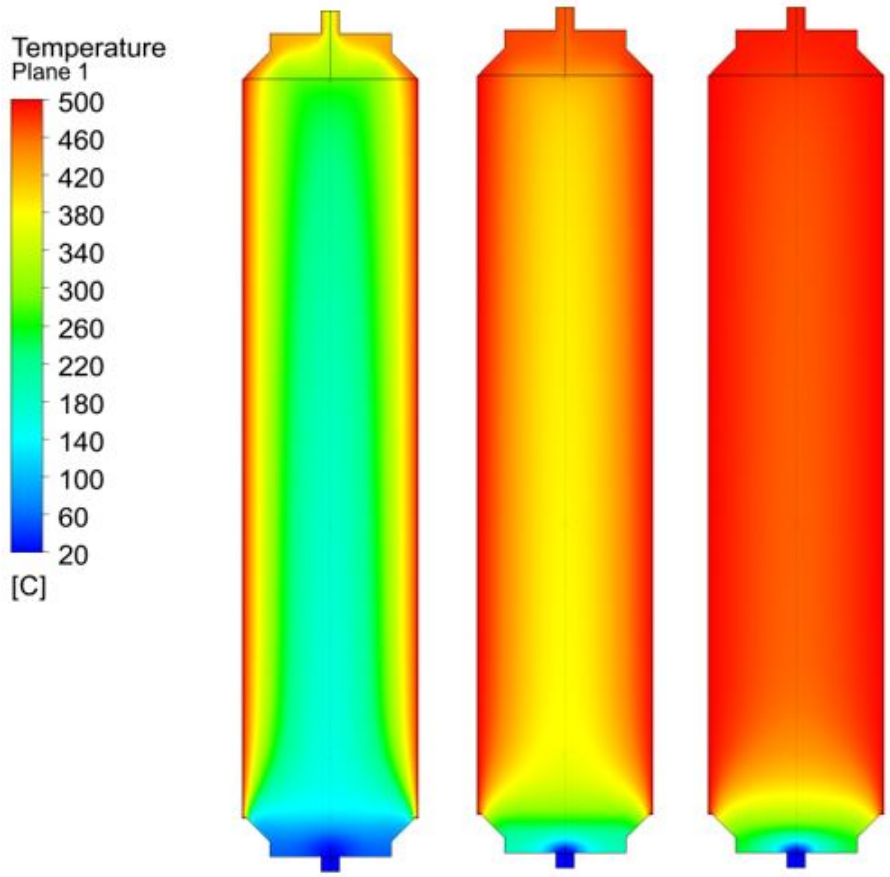

Figure 4.12: Contour plots of the reactor temperature during 3 different stages. From left to right: t = 37 min, 70 min and 100 min

The implications Fig. 4.12 have on a biomass conversion could be that the wood chips on the bottom will have a slower conversion rate that the ones on top. Possibly, the wood chips might not be completely pyrolyzed given the operating conditions chosen for this case. A more uniform pyrolysis process could be achieved if the inlet gas were preheated in order to avoid too large temperature differences. Alternatively, numerical tests including new or established reactor designs could be expedient if a cold gas inlet is the requirement.

Chapter 5

Conclusion

This research aimed to uncover the mass and heat transfer mechanisms in wood pyrolysis. CFD was used to simulate the process numerically. The method of creating cases was a well-ordered approach to study how assumptions, choice of empirical correlations, boundary conditions and source terms affect the results. Based the on step-wise approach used to arrive to the working model, the following points can be summed up as the final take away:

The mass source temperature function created a satisfying total mass loss although it was formulated quite simply. By choosing an "on-or-off" function, the desired mass loss rate with respect to time was also achieved. This shows that the source still can be of a constant value, however some more limitations should be added to the function in order to be more physically sound. Alternatively, as it was somewhat numerically and physically flawed the function should be replaced in favor to that of a sinusoidal curve.

The porous domain proved to create a considerable momentum sink. The pressure loss of the porous domain was considered insignificant. This claim can also be supported by literature or from empirical correlations.

The models were able to capture the transient heat transfer and the buoyancy effects quite well. The contours of the energy balance seemed to be in order, however the accuracy of the heat transfer rates was doubtful. The results that implied that the heat transfer rates between the solid and gas phase was taken to be zero is quite uncertain. The results focusing on the increase in domain temperature turned out to agree well with the expectations.

The method used was, as mentioned, a very neat strategy to identify weakness along the process and to understand the impact on each choice. This was a good help to prevent too many unknown issues appearing at the same time, as a direct approach possibly could. Also, by anticipating major flow parameters with the help of fundamental theory was a good method the evaluate the credibility of the results. The theoretical hand-calculations were in general, but not at all times, in good agreement with the numerical ones. Depending on the areas of interest, the models showed it is possible to describe pyrolysis with solely transient heat and mass transfer mechanisms. Evidently, a true computational model of pyrolysis extends transient heat and mass transfer as chemical kinetics should be an integral part of a numerical pyrolysis model.

Chapter 6

Further Work

The working model can be further improved. As time and computational resources limited the work, not all the desired configurations got the chance to be included in the numerical models. The results also raised new questions that can be the starting point of new studies. Following is a list of points that include improvement of the current models and areas to for further study:

As previously discussed, the mass source term should be improved. The temperature relation of the mass source should ideally be defined by a continuous curve. Additionally, the mass of wood should be coupled to the mass flow rate that leave the reactor. That way, more physics is included in the model, and consequently the model becomes more versatile for varying operating conditions.

More gas species can be included in order to portray a more correct volatilization. The work on the volatile gases would, as individual mass sources, include UDFs that prescribe species temperature functions according to that discussed in the previous paragraph. The thermodynamic properties such as density, specific heat capacity and thermal conductivity of each species should also be defined individually, and according to what can found from thermodynamic data tables.

Similarly, more work on the wood thermodynamic properties should be done. Variables, e.g. specific heat capacity and density, could be programmed to gradually change towards that of biochar. By changing these variables, the rate at which the reactor is heated is expected to increase. Thus, it is likely to think that a steady state solution is obtained faster.

A new look at the porosity formulation can also be done. By reviewing more literature, a proper formulation that take the anisotropy of wood chips into consideration can be obtained. As a result, new temperature distribution plots and possibly new flow patterns might be introduced. Improvements work should also be done to understand more of the non-thermal equilibrium source between the gas and solid phase.

By running a parametric study of the main operating conditions, such as particle size or heating rate, a frame of reference is obtained that will to some extent evaluate the energy efficiency the current one. As Elkem explores the possibility of biomass conversion, naturally the conversion should be as energy efficient and economical as possible. The pyrolysis process depends on a range of parameters, therefore the optimization potential can be great.

Bibliography

[1] B.R. Meyer et al. *Modeling of proppant permeability and inertial factor for fluid flow through packed columns*. International Society for Rock Mechanics and Rock Engineering, 2013.

[2] M. Alaqqad, C.P.J. Bennington, and D.M. Martinez. "The permeability of wood-chip beds: The effect of compressibility". eng. In: *Canadian Journal of Chemical Engineering* 90.5 (2012), pp. 1278–1288. ISSN: 0008-4034.

[3] ANSYS. *Fluent Theory Guide*. Chap. 1.2.1. The Mass Conservation Equation.

[4] ANSYS. *Fluent Theory Guide*. Chap. 5.2.1.1 The Energy Equation.

[5] ANSYS. *Fluent Theory Guide*. Chap. 7.1.1. Species Transport Equations.

[6] ANSYS. *Fluent User's Guide*. Chap. 6.2.3.7.6. Defining the Viscous and Inertial Resistance Coefficients.

[7] ANSYS. *Fluent User's Guide*. Chap. 6.2.3.4 Treatment of the Energy Equation in Porous Media.

[8] ANSYS. *Fluent User's Guide*. Chap. 12.2.4.6. Solution Strategies for Buoyancy-Driven Flows.

[9] M. Antal and M. Gronli. "The art, science, and technology of charcoal production". English. In: *Industrial Engineering Chemistry Research* 42.8 (2003), pp. 1619–1640. ISSN: 0888-5885.

[10] ASTM. *Standard Test Method for Volatile Matter in the Analysis of Particulate Wood Fuels*. URL: `https://www.astm.org/Standards/E872.htm`. (accessed: 24.08.2019).

[11] B.V. Babu. "Biomass pyrolysis: a state-of-the-art review". In: *Biofuels, Bioproducts and Biorefining: Innovation for a sustainable economy* 2.5 (2008), pp. 393–414.

[12] P. Basu. *Biomass gasification and pyrolysis : practical design and theory*. eng. Amsterdam: Elsevier, 2010. Chap. 3.6 Composition of biomass. ISBN: 9780123749888.

[13] P. Basu. *Biomass gasification and pyrolysis : practical design and theory*. eng. Amsterdam: Elsevier, 2010. Chap. 3.3.1 Structure of wood. ISBN: 9780123749888.

[14] P. Basu. *Biomass gasification and pyrolysis : practical design and theory*. eng. Amsterdam: Elsevier, 2010. Chap. 5.2 Pyrolysis. ISBN: 9780123749888.

[15] P. Basu. *Biomass gasification and pyrolysis : practical design and theory*. eng. Amsterdam: Elsevier, 2010. Chap. 3.5 Properties of Biomass. ISBN: 9780123749888.

[16] S. E. Boslaugh. *Pyrolysis*. URL: https://www.britannica.com/science/pyrolysis. (accessed: 24.08.2019).

[17] *Canadian woods, their properties and uses*. eng. Toronto, Ont. ; 1981.

[18] A.P.S. Chouhan and A.K. Sarma. "Critical analysis of process parameters for bio-oil production via pyrolysis of biomass: A review". In: *Recent Patents on Engin* 7 (2013), pp. 1–17.

[19] L.E. Christianson et al. *Technical Note: Hydraulic Property Determination of Denitrifying Bioreactor Fill Media*.

[20] United Nations Framework Convention on Climate Change. *Nationally Determined Contributions (NDCs)*. URL: https://unfccc.int/process-and-meetings/the-paris-agreement/nationally-determined-contributions-ndcs. (accessed: 24.08.2019).

[21] Ministry of Climate and Environment. *Lov om klimamål (klimaloven)*. URL: https://lovdata.no/dokument/NL/lov/2017-06-16-60. (accessed: 24.08.2019).

[22] Ministry of Climate and Environment. *Norwegian Carbon Credit Procurement Program*. URL: https://www.regjeringen.no/en/topics/climate-and-environment/climate/innsiktsartikler-klima/norwegian-carbon-credit-procurement-program/id2415405/. (accessed: 24.08.2019).

[23] United Nations Treaty Collection. *7. d Paris Agreement*. URL: https://treaties.un.org/Pages/ViewDetails.aspx?src=TREATY&mtdsg_no=XXVII-7-d&chapter=27&lang=_en&clang=_en. (accessed: 24.08.2019).

[24] European Commission. *2030 climate energy framework*. URL: https://ec.europa.eu/clima/policies/strategies/2030_en. (accessed: 24.08.2019).

[25] European Commission. *2050 Energy Strategy*. URL: https://ec.europa.eu/energy/en/topics/energy-strategy-and-energy-union/2050-energy-strategy. (accessed: 24.08.2019).

[26] European Commission. *EU Emissions Trading System (EU ETS)*. URL: https://ec.europa.eu/clima/policies/ets_en. (accessed: 24.08.2019).

[27] A. Demirbaş. "Relationships between Carbonization Temperature and Pyrolysis Products from Biomass". eng. In: 22.6 (2004), pp. 411–419. ISSN: 0144-5987.

[28] *Determination Of Total Content Of Carbon, Hydrogen And Nitrogen - Instrumental Methods*. URL: https://webstore.ansi.org/standards/din/dinen151042011. (accessed: 24.08.2019).

[29] C. Di Blasi. "Modeling chemical and physical processes of wood and biomass pyrolysis". eng. In: *Progress in Energy and Combustion Science* 34.1 (2008), pp. 47–90. ISSN: 0360-1285.

[30] M. Dolmen. *ØKT BRUK AV BIOKARBON FOR LAVKARBONSAMFUNNET*. URL: https://docplayer.me/105005509-Okt-bruk-av-biokarbon-for-lavkarbonsamfunnet-marit-dolmen.html. (accessed: 24.08.2019).

[31] C. A. Eckelman. *Wood Moisture Calculations*. URL: https://www.extension.purdue.edu/extmedia/FNR/FNR-156.pdf. (accessed: 24.08.2019).

[32] Elkem. *Elkem GRI report*. 2017. URL: https://www.elkem.com/sustainability/sustainability-reports/sustainability-reporting-2017/.

[33] Elkem. *Elkem's environmental and energy strategy*. URL: https://www.elkem.com/sustainability/elkems-environmental-and-energy-strategy/. (accessed: 24.08.2019).

[34] Elkem. *Veien til klimanøytral metallproduksjon*. URL: https://www.elkem.com/no/innovasjon/langsiktig-fou/veien-til-klimanoytral-metallproduksjon/. (accessed: 24.08.2019).

[35] Ministry of Foreign Affairs. *Norges miljø- og klimasamarbeid med EU*. URL: https://www.regjeringen.no/no/tema/europapolitikk/tema/miljo-og-klima1/id686218/. (accessed: 24.08.2019).

[36] W. A. González et al. "Numerical analysis of wood biomass packing factor in a fixed-bed gasification process". eng. In: *Renewable Energy* 121 (2018), pp. 579–589. ISSN: 0960-1481.

[37] W.P. Goss and R.G. Miller. *Thermal properties of wood and wood products*. 1992.

[38] T. Grace. *Porosity and Permeability*. URL: https://www.classzone.com/books/earth_science/terc/content/investigations/es1401/es1401page04.cfm. (accessed: 24.08.2019).

[39] E. Grieco and G. Baldi. "Analysis and modelling of wood pyrolysis". eng. In: *Chemical engineering science* 66.4 (2011), pp. 650–660. ISSN: 0009-2509.

[40] M.G. Grønli. *A theoretical and experimental study of the thermal degradation of biomass*. eng. Trondheim, 1996.

[41] M. Gupta, J Yang, and C. Roy. "Specific heat and thermal conductivity of softwood bark and softwood char particles ". eng. In: *Fuel* 82.8 (2003), pp. 919–927. ISSN: 0016-2361.

[42] S. Hamel and W. Krumm. "Near-wall porosity characteristics of fixed beds packed with wood chips". eng. In: 188.1 (2008), pp. 55–63. ISSN: 0032-5910.

[43] Y. Haseli, J.A. van Oijen, and L.P.H. de Goey. "Modeling biomass particle pyrolysis with temperature-dependent heat of reactions". eng. In: 90.2 (2011), pp. 140–154. ISSN: 0165-2370.

[44] K. Henning and H. Kienle. "Activated Carbon". In: (). URL: https://onlinelibrary.wiley.com/doi/10.1002/14356007.n05_n04. (accessed: 24.08.2019).

[45] C.S. Ima and D.D. Mann. "Hygroscopic expansion of biofilter media consisting of woodchips.(Report)". English. In: *Australian Journal of Agricultural Engineering* 2.1 (2011). ISSN: 1836-943X.

[46] Norsk Industri. *Elkem får tilsagn på over 40 millioner kroner fra Forskningsrådet*. URL: https://www.norskindustri.no/dette-jobber-vi-med/forskning-og-innovasjon/aktuelt/elkem-far-tilsagn-pa-over-40-millioner-kroner-fra-forskningsradet/. (accessed: 24.08.2019).

[47] B.M. Jenkins. "Physical properties of biomass". In: *Biomass handbook* (1989), pp. 860–891.

[48] S. Kersten and M. Garcia-Perez. "Recent developments in fast pyrolysis of ligno-cellulosic materials". eng. In: *Current Opinion in Biotechnology* 24.3 (2013), pp. 414–420. ISSN: 0958-1669.

[49] H.S. Kol. "Thermal and dielectric properties of pine wood in the transverse direction". In: *BioResources* 4.4 (2009), pp. 1663–1669. ISSN: 19302126.

[50] F. F.P. Kollmann and W.A. Côté. *Principles of Wood Science and Technology: I Solid Wood*. eng. Berlin, Heidelberg: Springer Berlin Heidelberg, 1968. Chap. 6.5 Thermal Properties of Wood. ISBN: 9783642879289.

[51] D. Kurz, U. Schnell, and G. Scheffknecht. "CFD simulation of wood chip combustion on a grate using an Euler–Euler approach". In: *Combustion Theory and Modelling* 16.2 (2012), pp. 251–273. ISSN: 1364-7830.

[52] Bosong L. et al. "Pyrolysis and catalytic upgrading of pine wood in a combination of auger reactor and fixed bed". English. In: *Fuel* 129 (2014), p. 61. ISSN: 0016-2361.

[53] K. L. Lam, A. O. Oyedun, and C. W. Hui. "Experimental and Modelling Studies of Biomass Pyrolysis". eng. In: *Chinese Journal of Chemical Engineering* 20.3 (2012), pp. 543–550. ISSN: 1004-9541.

[54] A.L Lunguleasa, C. Cosereanu, and D. Lica. *Method for determining the specific area of chips*. 2009.

[55] J. Manya. "Pyrolysis for Biochar Purposes: A Review to Establish Current Knowledge Gaps and Research Needs". English. In: *Environmental Science Technology* 46.15 (2012), pp. 7939–7954. ISSN: 0013-936X.

[56] M. Mayerhofer et al. "Experimental investigation of pressure drop in packed beds of irregular shaped wood particles". eng. In: *Powder Technology* 205.1 (2011), pp. 30–35. ISSN: 0032-5910.

[57] R.S. Miller and J. Bellan. "A Generalized Biomass Pyrolysis Model Based on Superimposed Cellulose, Hemicelluloseand Liqnin Kinetics". In: *Combustion Science and Technology* 126.1-6 (1997), pp. 97–137. ISSN: 0010-2202.

[58] I. Milosavljevic, V. Oja, and E.M. Suuberg. "Thermal effects in cellulose pyrolysis: Relationship to char formation processes". English. In: 35.3 (1996), pp. 653–662. ISSN: 0888-5885.

[59] United Nations. *Paris Agreement*. URL: `https://unfccc.int/files/essential_background/convention/application/pdf/english_paris_agreement.pdf`. (accessed: 24.08.2019).

[60] D. Neves et al. "Characterization and prediction of biomass pyrolysis products". eng. In: 37.5 (2011), pp. 611–630. ISSN: 0360-1285.

[61] P.O. Okekunle et al. "Numerical and Experimental Investigation of Intra-Particle Heat Transfer and Tar Decomposition during Pyrolysis of Wood Biomass". eng. In: *Journal of Thermal Science and Technology* 6.3 (2011). ISSN: 18805566. URL: `http://search.proquest.com/docview/1466130414/`.

[62] V. Pozzobon, J. Colin, and P. Perré. "Hydrodynamics of a packed bed of non-spherical polydisperse particles: A fully virtual approach validated by experiments". eng. In: *Chemical Engineering Journal* 354 (2018), pp. 126–136. ISSN: 1385-8947.

[63] K. Radmanović, I. Đukić, and S. Pervan. *Specific Heat Capacity of Wood*. 2014.

[64] K.W. Ragland, D.J. Aerts, and A.J. Baker. "Properties of wood for combustion analysis". eng. In: *Bioresource Technology* 37.2 (1991), pp. 161–168. ISSN: 0960-8524.

[65] J. Rath et al. "Heat of wood pyrolysis". eng. In: *Fuel* 82.1 (2003), pp. 81–91. ISSN: 0016-2361.

[66] B. Saletnik et al. "Biochar as a multifunctional component of the environment-a review". In: *Applied Sciences (Switzerland)* 9.6 (2019). ISSN: 20763417.

[67] C. Sapia and G. Sozio. "CFD transient model of the natural convection heat transfer for an heat sink effects of increasing surface and fins spacing". eng. In: *2011 17th International Workshop on Thermal Investigations of ICs and Systems (THERMINIC)*. IEEE, 2011, pp. 1–6. ISBN: 9781457707780.

[68] S. Şensöz and M. Can. "Pyrolysis of Pine (Pinus Brutia Ten.) Chips: 1. Effect of Pyrolysis Temperature and Heating Rate on the Product Yields". In: *Energy Sources* 24.4 (2002), pp. 347–355. ISSN: 0090-8312.

[69] D. Shepard. *Paris Climate Agreement to enter into force on 4 November*. URL: `https://www.un.org/sustainabledevelopment/blog/2016/10/paris-climate-agreement-to-enter-into-force-on-4-november/`. (accessed: 24.08.2019).

[70] X. Shi, F. Ronsse, and J. G. Pieters. "Finite element modeling of intraparticle heterogeneous tar conversion during pyrolysis of woody biomass particles". eng. In: *Fuel Processing Technology* 148 (2016), pp. 302–316. ISSN: 0378-3820.

[71] E. Sjöström. *Wood chemistry : fundamentals and applications*. eng. 2nd ed. New York: Academic Press, 1993. Chap. 10.1.3 Thermal Treatment. ISBN: 0126474818.

[72] H. Ström and H. Thunman. "CFD simulations of biofuel bed conversion: A submodel for the drying and devolatilization of thermally thick wood particles". eng. In: *Combustion and Flame* 160.2 (2013), pp. 417–431. ISSN: 0010-2180.

[73] K. Tannous et al. "Physical Properties for Flow Characterization of Ground Biomass from Douglas Fir Wood". eng. In: *Particulate Science and Technology* 31.3 (2013), pp. 291–300. ISSN: 0272-6351.

[74] *Thermal properties of wood*. URL: `https://www.woodproducts.fi/content/wood-a-material-2`. (accessed: 24.08.2019).

[75] Engineering Toolbox. *Thermal Conductivity of common Materials and Gases*. URL: `https://www.engineeringtoolbox.com/thermal-conductivity-d_429.html`. (accessed: 24.08.2019).

[76] T.Radó. "On Surface Area." In: *Proceedings of the National Academy of Sciences of the United States of America* 31 3 (1945), pp. 102–6.

[77] I. Usta. "Comparative study of wood density by specific amount of void volume (porosity)". In: *Turkish Journal of Agriculture and Forestry* 27.1 (2003), pp. 1–6. ISSN: 1300011X.

[78] H.K Versteeg. *An introduction to computational fluid dynamics : the finite volume method*. eng. Harlow, 2007.

[79] Y. Wang et al. “Effects of different heating patterns on the decomposition behavior of white pine wood during slow pyrolysis”. English. In: *International Journal Of Agricultural And Biological Engineering* 11.5 (2018), pp. 218–223. ISSN: 1934-6344.

[80] P.T. Williams and S. Besler. “The influence of temperature and heating rate on the slow pyrolysis of biomass”. eng. In: *Renewable Energy* 7.3 (1996), pp. 233–250. ISSN: 0960-1481.

[81] European Wood. *Thermal Conductivity*. URL: `https://www.europeanwood.org.cn/en/thermal-properties`. (accessed: 24.08.2019).

[82] C. Wu et al. “Conventional and microwave-assisted pyrolysis of biomass under different heating rates”. eng. In: *Journal of Analytical and Applied Pyrolysis* 107.C (2014). ISSN: 01652370.

[83] Q. Yan et al. “Effects of pyrolysis conditions on yield of bio-chars from pine chips”. English. In: *Forest Products Journal* 61.5 (2011). ISSN: 0015-7473.

[84] H. Yang et al. “In-depth investigation of biomass pyrolysis based on three major components: Hemicellulose, cellulose and lignin”. In: *Energy and Fuels* 20.1 (2006), pp. 388–393. ISSN: 08870624.

[85] E. Ydstie. *From Sand to Silicon Wafers: A Process Systems view of Solar Cell Production*. URL: `http://egon.cheme.cmu.edu/esi/docs/pdf/10_EIS_Solar_Overview_Erik_2014.pdf`. (accessed: 24.08.2019).

Appendix

A

Parameters of Case 4 geometry

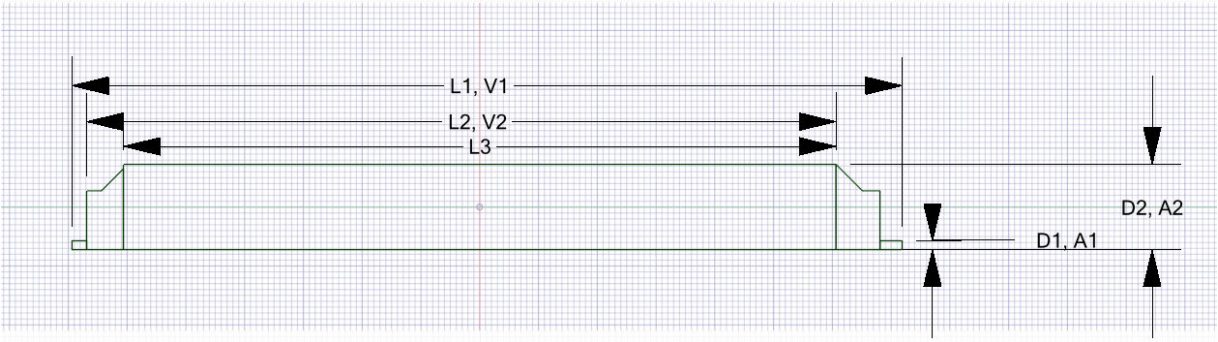

B.1

Mesh Figures from top to bottom: Outlet, Inlet.

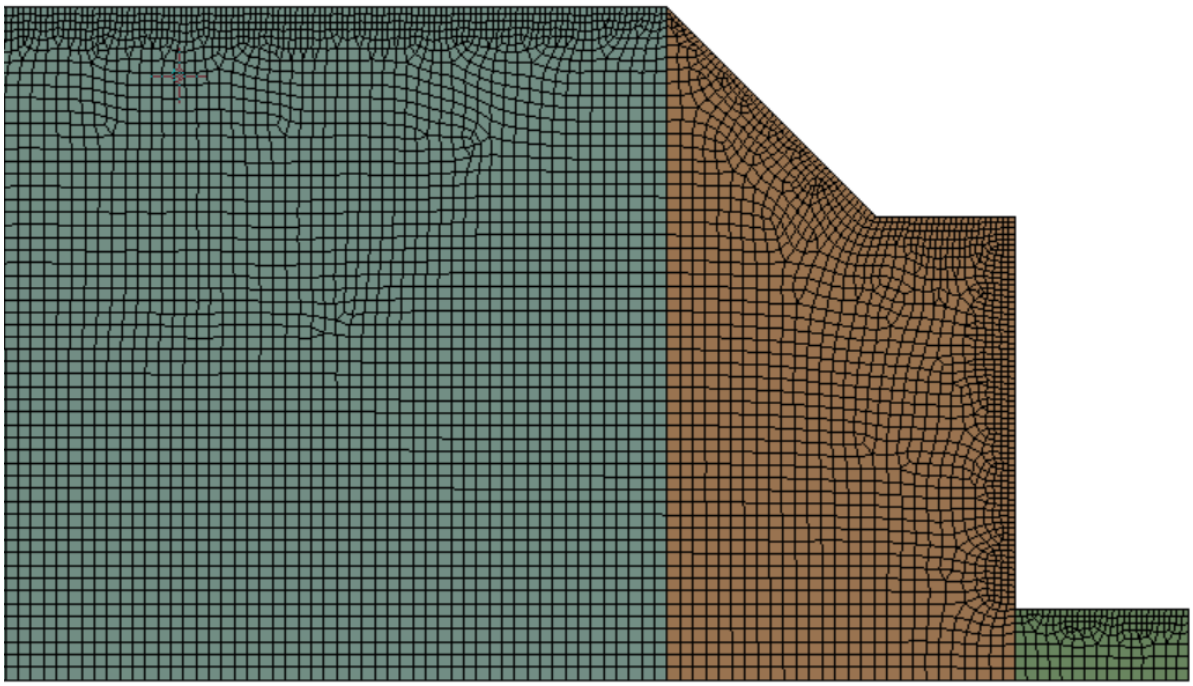

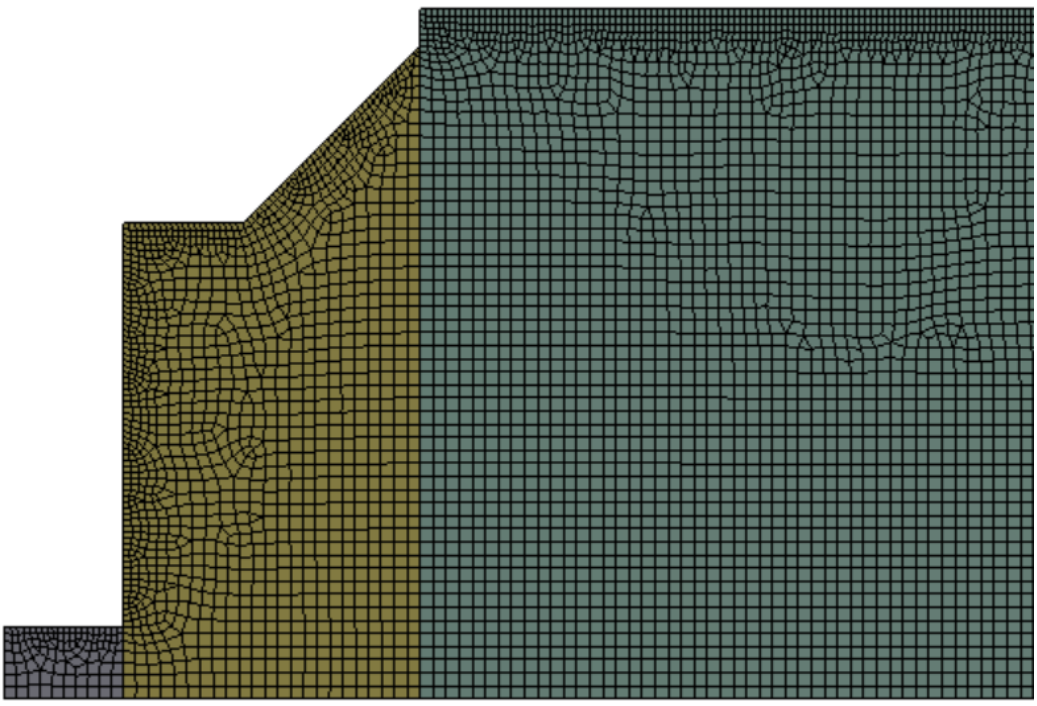

B.2

Mesh report from model used in Case 1, 2 and 3.

First Saved	Sunday, August 11, 2019
Last Saved	Saturday, August 17, 2019
Product Version	19.0 Release
Imported Source	C:\Users\abelma\Documents\ANSYS\Canvas\case123mesh.meshdat
Imported Version	19.0 Release
Save Project Before Solution	No
Save Project After Solution	No

Contents

Units

TABLE 1

Unit System	Metric (mm, t, N, s, mV, mA) Degrees rad/s Celsius
Angle	Degrees
Rotational Velocity	rad/s
Temperature	Celsius

Model (A3)

Geometry

TABLE 2
Model (A3) > Geometry

Object Name	*Geometry*
State	Fully Defined
Definition	
Source	C:\Users\abelma\OD\Master Thesis\ANSYS\work_files\dp0\SYS\DM\SYS.scdoc
Type	SpaceClaim
Length Unit	Meters
Bounding Box	
Length X	555, mm
Length Y	58, mm
Length Z	1,9895e-013 mm

Properties	
Volume	0, mm³
Surface Area(approx.)	30696 mm²
Scale Factor Value	1,
Statistics	
Bodies	4
Active Bodies	4
Nodes	31785
Elements	31047
Mesh Metric	Orthogonal Quality
Min	0,609353860591167
Max	1
Average	0,991718750180007
Standard Deviation	2,57465254715753E-02
Basic Geometry Options	
Solid Bodies	Yes
Surface Bodies	Yes
Line Bodies	Yes
Parameters	Independent
Parameter Key	
Attributes	Yes
Attribute Key	
Named Selections	Yes
Named Selection Key	
Material Properties	Yes
Advanced Geometry Options	
Use Associativity	Yes
Coordinate Systems	Yes
Coordinate System Key	

Reader Mode Saves Updated File	No
Use Instances	Yes
Smart CAD Update	Yes
Compare Parts On Update	No
Analysis Type	3-D
Mixed Import Resolution	None
Decompose Disjoint Geometry	Yes
Enclosure and Symmetry Processing	Yes

TABLE 3
Model (A3) > Geometry > Body Groups

Object Name	*Geom*
State	Meshed
Graphics Properties	
Visible	Yes
Definition	
Suppressed	No
Assignment	
Coordinate System	Default Coordinate System
Bounding Box	
Length X	555, mm
Length Y	58, mm
Length Z	1,9895e-013 mm
Properties	
Volume	0, mm³
Surface Area(approx.)	30696 mm²
Statistics	
Nodes	31785
Elements	31047

Mesh Metric	Orthogonal Quality
Min	0,609353860591167
Max	1
Average	0,991718750180007
Standard Deviation	2,57465254715753E-02
CAD Attributes	
PartTolerance:	0,00000001
Color:143.175.143	

TABLE 4
Model (A3) > Geometry > Geom > Parts

Object Name	*Surface1*	*Surface2*	*Surface3*	*Surface4*
State	Meshed			
Graphics Properties				
Visible	Yes			
Transparency	1			
Definition				
Suppressed	No			
Coordinate System	Default Coordinate System			
Thickness	0, mm			
Thickness Mode	Refresh on Update			
Offset Type	Middle			
Behavior	None			
Reference Frame	Lagrangian			
Material				
Assignment				
Fluid/Solid	Defined By Geometry (Solid)			
Bounding Box				

Length X	15, mm	30, mm	485, mm	25, mm
Length Y	6,096 mm	58, mm		55, mm
Length Z	2,1782e-014 mm	1,9895e-013 mm		1,8866e-013 mm
Properties				
Volume	0, mm³			
Centroid X	547,5 mm	523,93 mm	267,5 mm	13,258 mm
Centroid Y	3,048 mm	23,093 mm	29, mm	22,528 mm
Centroid Z	-8,6444e-014 mm	-1,7808e-014 mm	2,3328e-015 mm	-1,9868e-014 mm
Surface Area(approx.)	91,44 mm²	1362, mm²	28130 mm²	1112,5 mm²
Statistics				
Nodes	197	1762	28378	1567
Elements	168	1651	27761	1467
Mesh Metric	Orthogonal Quality			
Min	0,881873843119503	0,73087016461874	0,609353860591167	0,627678557417249
Max	0,999998673445296	0,999999874725426	1	0,999999569524975
Average	0,976204603947281	0,980685299211866	0,992993487523714	0,981790066278753
Standard Deviation	2,75343238886635E-02	3,30451004582518E-02	2,40854044907754E-02	3,79972550485638E-02

Coordinate Systems

TABLE 5
Model (A3) > Coordinate Systems > Coordinate System

Object Name	*Global Coordinate System*
State	Fully Defined
Definition	
Type	Cartesian
Coordinate System ID	0,
Origin	
Origin X	0, mm

Origin Y	0, mm
Origin Z	0, mm
Directional Vectors	
X Axis Data	[1, 0, 0,]
Y Axis Data	[0, 1, 0,]
Z Axis Data	[0, 0, 1,]

Connections

TABLE 6
Model (A3) > Connections

Object Name	*Connections*
State	Fully Defined
Auto Detection	
Generate Automatic Connection On Refresh	Yes
Transparency	
Enabled	Yes

Mesh

TABLE 7
Model (A3) > Mesh

Object Name	*Mesh*
State	Solved
Display	
Display Style	Body Color
Defaults	
Physics Preference	CFD
Solver Preference	Fluent
Export Format	Standard
Export Preview Surface Mesh	No
Element Order	Linear
Sizing	

Size Function	Curvature
Max Face Size	1,10 mm
Mesh Defeaturing	Yes
Defeature Size	Default (5,5e-003 mm)
Growth Rate	Default (1,20)
Min Size	Default (1,1e-002 mm)
Curvature Normal Angle	Default (18,0 °)
Bounding Box Diagonal	558,020 mm
Average Surface Area	7674,0 mm²
Minimum Edge Length	3,0 mm
Quality	
Check Mesh Quality	Yes, Errors
Target Skewness	Default (0.900000)
Smoothing	Medium
Mesh Metric	Orthogonal Quality
Min	0,60935
Max	1,
Average	0,99172
Standard Deviation	2,5747e-002
Mesh Metric	Skewness
Min	0,60935
Max	1,
Average	0,99172
Standard Deviation	2,5747e-002
Inflation	
Use Automatic Inflation	None
Inflation Option	Smooth Transition
Transition Ratio	0,272
Maximum Layers	2

Growth Rate	1,2
Inflation Algorithm	Pre
View Advanced Options	No
Assembly Meshing	
Method	None
Advanced	
Number of CPUs for Parallel Part Meshing	Program Controlled
Straight Sided Elements	
Number of Retries	0
Rigid Body Behavior	Dimensionally Reduced
Triangle Surface Mesher	Program Controlled
Topology Checking	Yes
Use Sheet Thickness for Pinch	No
Pinch Tolerance	Default (9,9e-003 mm)
Generate Pinch on Refresh	No
Sheet Loop Removal	No
Statistics	
Nodes	31785
Elements	31047

TABLE 8
Model (A3) > Mesh > Mesh Controls

Object Name	*Edge Sizing*	*Face Sizing*
State	Fully Defined	
Scope		
Scoping Method	Geometry Selection	
Geometry	9 Edges	1 Face
Definition		
Suppressed	No	
Type	Element Size	

Element Size	0,5 mm	1,0 mm
Advanced		
Size Function	Uniform	
Behavior	Soft	
Growth Rate	Default (1,2)	
Bias Type	No Bias	
Defeature Size		Default (5,5e-003 mm)

B.3

Mesh report for Case 4.

First Saved	Sunday, August 11, 2019
Last Saved	Tuesday, August 13, 2019
Product Version	19.0 Release
Save Project Before Solution	No
Save Project After Solution	No

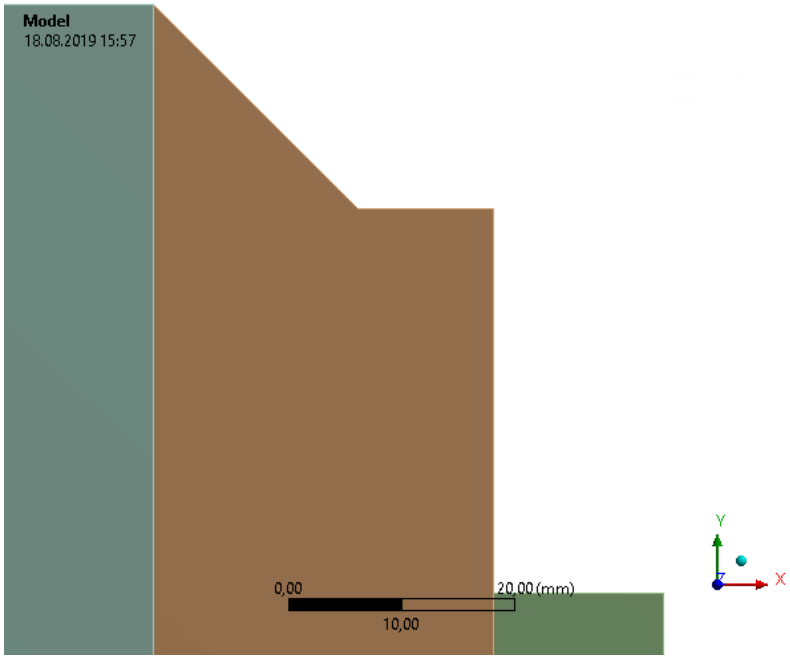

Contents

Units

TABLE 1

Unit System	Metric (mm, t, N, s, mV, mA) Degrees rad/s Celsius
Angle	Degrees
Rotational Velocity	rad/s
Temperature	Celsius

Model (B3)

Geometry

TABLE 2
Model (B3) > Geometry

Object Name	*Geometry*
State	Fully Defined
Definition	
Source	C:\Users\abelma\Documents\ANSYS\Canvas\Final_files\dp0\Geom\DM\Geom.scdoc
Type	SpaceClaim
Length Unit	Meters
Bounding Box	
Length X	565, mm
Length Y	58, mm
Length Z	1,9895e-013 mm
Properties	
Volume	0, mm³
Surface Area(approx.)	30757 mm²
Scale Factor Value	1,
Statistics	
Bodies	5
Active Bodies	5
Nodes	31543

Elements	30785
Mesh Metric	None
Basic Geometry Options	
Solid Bodies	Yes
Surface Bodies	Yes
Line Bodies	Yes
Parameters	Independent
Parameter Key	
Attributes	Yes
Attribute Key	
Named Selections	Yes
Named Selection Key	
Material Properties	Yes
Advanced Geometry Options	
Use Associativity	Yes
Coordinate Systems	Yes
Coordinate System Key	
Reader Mode Saves Updated File	No
Use Instances	Yes
Smart CAD Update	Yes
Compare Parts On Update	No
Analysis Type	3-D
Mixed Import Resolution	None
Decompose Disjoint Geometry	Yes
Enclosure and Symmetry Processing	Yes

TABLE 3
Model (B3) > Geometry > Body Groups

Object Name	*Geom*
State	Meshed
Graphics Properties	
Visible	Yes
Definition	
Suppressed	No
Assignment	
Coordinate System	Default Coordinate System
Bounding Box	
Length X	565, mm

Length Y	58, mm
Length Z	1,9895e-013 mm
Properties	
Volume	0, mm³
Surface Area(approx.)	30757 mm²
Statistics	
Nodes	31543
Elements	30785
Mesh Metric	None
CAD Attributes	
PartTolerance:	0,00000001
Color:143.175.143	

TABLE 4
Model (B3) > Geometry > Geom > Parts

Object Name	*Surface1*	*Surface2*	*Surface3*	*Surface4*	*Surface5*
State	Meshed				
Graphics Properties					
Visible	Yes				
Transparency	1				
Definition					
Suppressed	No				
Coordinate System	Default Coordinate System				
Thickness	0, mm				
Thickness Mode	Refresh on Update				
Offset Type	Middle				
Behavior	None				
Reference Frame	Lagrangian				
Material					
Assignment					
Fluid/Solid	Defined By Geometry (Solid)				
Bounding Box					
Length X	15, mm	30, mm	485, mm	25, mm	10, mm
Length Y	6,096 mm	58, mm		55, mm	6,096 mm
Length Z	2,0911e-014 mm	1,9895e-013 mm		1,8866e-013 mm	2,0911e-014 mm
Properties					
Volume	0, mm³				
Centroid X	547,5 mm	523,93 mm	267,5 mm	13,258 mm	-5, mm
Centroid Y	3,048 mm	23,093 mm	29, mm	22,528 mm	3,048 mm
Centroid Z	-8,6689e-014 mm	-1,7931e-014 mm	2,3328e-015 mm	-1,9868e-014 mm	-8,6689e-014 mm
Surface Area(approx.)	91,44 mm²	1362, mm²	28130 mm²	1112,5 mm²	60,96 mm²
Statistics					
Nodes	194	1770	28128	1448	128
Elements	166	1665	27498	1350	106
Mesh Metric	None				

Coordinate Systems

TABLE 5
Model (B3) > Coordinate Systems > Coordinate System

Object Name	*Global Coordinate System*
State	Fully Defined
Definition	
Type	Cartesian
Coordinate System ID	0,
Origin	
Origin X	0, mm
Origin Y	0, mm
Origin Z	0, mm
Directional Vectors	
X Axis Data	[1, 0, 0,]
Y Axis Data	[0, 1, 0,]
Z Axis Data	[0, 0, 1,]

Connections

TABLE 6
Model (B3) > Connections

Object Name	*Connections*
State	Fully Defined
Auto Detection	
Generate Automatic Connection On Refresh	Yes
Transparency	
Enabled	Yes

Mesh

TABLE 7
Model (B3) > Mesh

Object Name	*Mesh*
State	Solved
Display	
Display Style	Body Color
Defaults	
Physics Preference	CFD
Solver Preference	Fluent
Export Format	Standard
Export Preview Surface Mesh	No
Element Order	Linear
Sizing	
Size Function	Curvature
Max Face Size	1,10 mm
Mesh Defeaturing	Yes
Defeature Size	Default (5,5e-003 mm)

Growth Rate	Default (1,20)
Min Size	Default (1,1e-002 mm)
Curvature Normal Angle	Default (18,0 °)
Bounding Box Diagonal	567,970 mm
Average Surface Area	6151,40 mm²
Minimum Edge Length	3,0 mm
Quality	
Check Mesh Quality	Yes, Errors
Target Skewness	Default (0.900000)
Smoothing	Medium
Mesh Metric	None
Inflation	
Use Automatic Inflation	None
Inflation Option	Smooth Transition
Transition Ratio	0,272
Maximum Layers	2
Growth Rate	1,2
Inflation Algorithm	Pre
View Advanced Options	No
Assembly Meshing	
Method	None
Advanced	
Number of CPUs for Parallel Part Meshing	Program Controlled
Straight Sided Elements	
Number of Retries	0
Rigid Body Behavior	Dimensionally Reduced
Triangle Surface Mesher	Program Controlled
Topology Checking	Yes
Use Sheet Thickness for Pinch	No
Pinch Tolerance	Default (9,9e-003 mm)
Generate Pinch on Refresh	No
Sheet Loop Removal	No
Statistics	
Nodes	31543
Elements	30785

TABLE 8
Model (B3) > Mesh > Mesh Controls

Object Name	*Edge Sizing*	*Face Sizing*
State	Fully Defined	
Scope		
Scoping Method	Geometry Selection	
Geometry	10 Edges	2 Faces
Definition		
Suppressed	No	
Type	Element Size	
Element Size	0,5 mm	1,0 mm
Advanced		
Size Function	Uniform	

Behavior	Soft	
Growth Rate	Default (1,2)	
Bias Type	No Bias	
Defeature Size		Default (5,5e-003 mm)

Named Selections

TABLE 9
Model (B3) > Named Selections > Named Selections

Object Name	*cell_zone1*	*cell_zone2*	*cell_zone3*	*outlet*	*top*	*wall*	*bottom*	*inlet*	*symmetry_bottom*	*symmetry_top*
State	Fully Defined									
Scope										
Scoping Method	Geometry Selection									
Geometry	2 Bodies		1 Body	1 Edge	4 Edges	2 Edges	4 Edges	1 Edge	2 Edges	3 Edges
Definition										
Send to Solver	Yes									
Protected	Program Controlled									
Visible	Yes									
Program Controlled Inflation	Exclude									
Statistics										
Type	Manual									
Total Selection	2 Bodies		1 Body	1 Edge	4 Edges	2 Edges	4 Edges	1 Edge	2 Edges	3 Edges
Suppressed	0									
Used by Mesh Worksheet	No									
Length				6,096 mm	86,36 mm	488, mm	75,117 mm	6,096 mm	35, mm	530, mm

B.4

Mesh report for an equivalent 3D case.

First Saved	Saturday, August 17, 2019
Last Saved	Saturday, August 17, 2019
Product Version	19.0 Release
Save Project Before Solution	No
Save Project After Solution	No

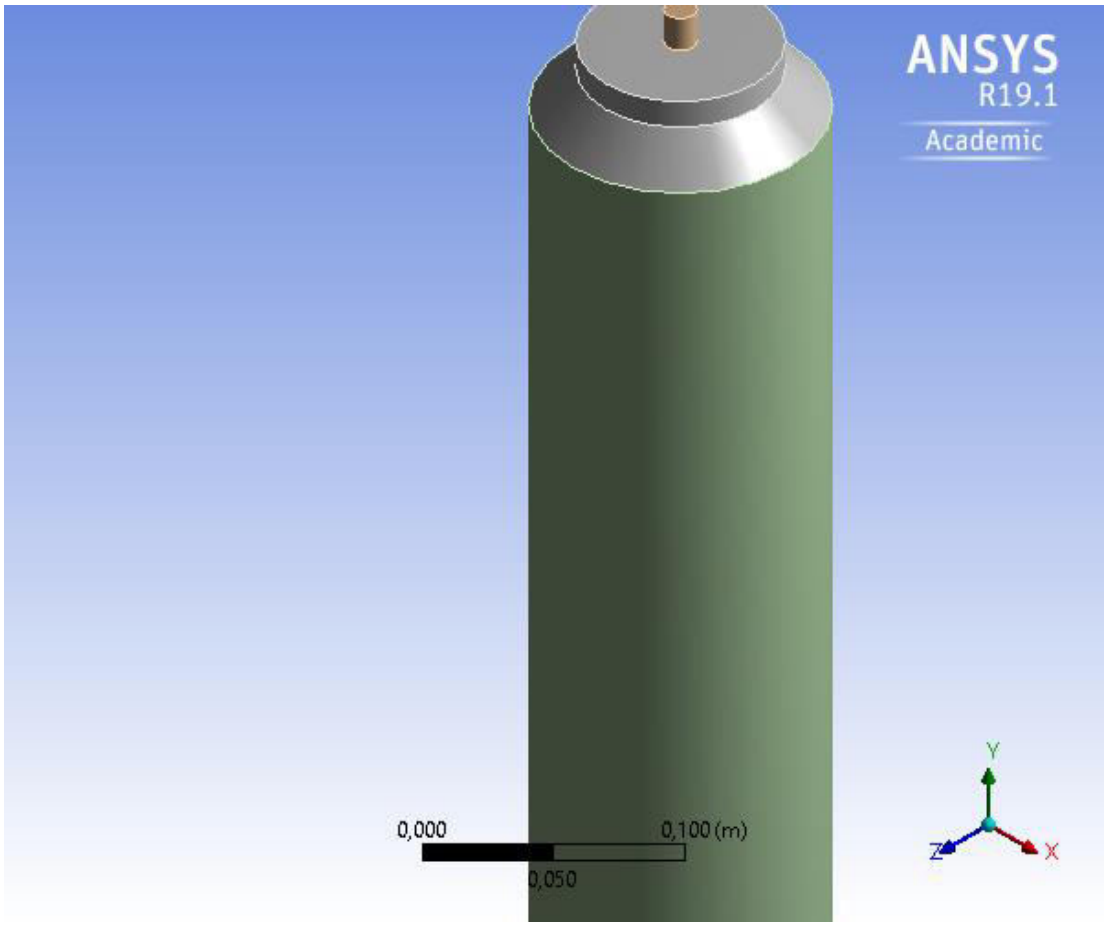

Contents

Units

TABLE 1

Unit System	Metric (m, kg, N, s, V, A) Degrees rad/s Celsius
Angle	Degrees
Rotational Velocity	rad/s
Temperature	Celsius

Model (B3)

Geometry

TABLE 2
Model (B3) > Geometry

Object Name	*Geometry*
State	Fully Defined
Definition	
Source	C:\Users\abelma\OneDrive - NTNU\Master Thesis\ANSYS\work_files\dp0\SYS-1\DM\SYS-1.scdoc
Type	SpaceClaim
Length Unit	Meters
Bounding Box	
Length X	0,116 m
Length Y	0,555 m
Length Z	0,116 m
Properties	
Volume	5,4826e-003 m³
Scale Factor Value	1,
Statistics	
Bodies	4
Active Bodies	4
Nodes	71915018
Elements	50352813
Mesh Metric	None
Update Options	
Assign Default Material	No
Basic Geometry Options	
Solid Bodies	Yes

Surface Bodies	Yes
Line Bodies	Yes
Parameters	Independent
Parameter Key	
Attributes	Yes
Attribute Key	
Named Selections	Yes
Named Selection Key	
Material Properties	Yes
Advanced Geometry Options	
Use Associativity	Yes
Coordinate Systems	Yes
Coordinate System Key	
Reader Mode Saves Updated File	No
Use Instances	Yes
Smart CAD Update	Yes
Compare Parts On Update	No
Analysis Type	3-D
Mixed Import Resolution	None
Decompose Disjoint Geometry	Yes
Enclosure and Symmetry Processing	Yes

TABLE 3
Model (B3) > Geometry > Body Groups

Object Name	*SYS-1*
State	Meshed
Graphics Properties	
Visible	Yes
Definition	
Suppressed	No
Assignment	
Coordinate System	Default Coordinate System
Bounding Box	
Length X	0,116 m
Length Y	0,555 m
Length Z	0,116 m
Properties	
Volume	5,4826e-003 m³
Statistics	
Nodes	71915018
Elements	50352813
Mesh Metric	None
CAD Attributes	
PartTolerance:	0,00000001
Color:143.175.143	

TABLE 4
Model (B3) > Geometry > SYS-1 > Parts

Object Name	*fluid_domain2*	*fluid_domain4*	*fluid_domain3*	*fluid_domain21*
State	Meshed			

Graphics Properties				
Visible	Yes			
Transparency	1			
Definition				
Suppressed	No			
Coordinate System	Default Coordinate System			
Behavior	None			
Reference Frame	Lagrangian			
Material				
Assignment				
Fluid/Solid	Defined By Geometry (Solid)			
Bounding Box				
Length X	0,116 m	0,11 m	0,116 m	1,27e-002 m
Length Y	3,e-002 m	2,5e-002 m	0,485 m	1,5e-002 m
Length Z	0,116 m	0,11 m	0,116 m	1,27e-002 m
Properties				
Volume	1,9762e-004 m³	1,5747e-004 m³	5,1256e-003 m³	1,9001e-006 m³
Centroid X	-6,2603e-011 m	9,9815e-011 m	1,2716e-018 m	-2,5511e-019 m
Centroid Y	-0,34818 m	-0,85696 m	-0,6035 m	-0,3235 m
Centroid Z	6,e-002 m			
Statistics				
Nodes	3327517	4263413	64319648	105187
Elements	2367447	1042146	46918320	24900
Mesh Metric	None			

Coordinate Systems

TABLE 5
Model (B3) > Coordinate Systems > Coordinate System

Object Name	*Global Coordinate System*
State	Fully Defined
Definition	
Type	Cartesian
Coordinate System ID	0,
Origin	
Origin X	0, m
Origin Y	0, m
Origin Z	0, m
Directional Vectors	
X Axis Data	[1, 0, 0,]
Y Axis Data	[0, 1, 0,]
Z Axis Data	[0, 0, 1,]

Connections

TABLE 6
Model (B3) > Connections

Object Name	*Connections*
State	Fully Defined
Auto Detection	
Generate Automatic Connection On Refresh	Yes
Transparency	

Enabled	Yes

Mesh

TABLE 7
Model (B3) > Mesh

Object Name	*Mesh*
State	Solved
Display	
Display Style	Body Color
Defaults	
Physics Preference	Mechanical
Element Order	Program Controlled
Element Size	1,1e-003 m
Sizing	
Use Adaptive Sizing	No
Growth Rate	1,2
Max Size	Default (2,2e-003 m)
Mesh Defeaturing	Yes
Defeature Size	Default (5,5e-006 m)
Capture Curvature	Yes
Curvature Min Size	Default (1,1e-005 m)
Curvature Normal Angle	Default (70,395°)
Capture Proximity	No
Bounding Box Diagonal	0,57874 m
Average Surface Area	1,5459e-002 m²
Minimum Edge Length	3,9898e-002 m
Quality	
Check Mesh Quality	Yes, Errors
Error Limits	Standard Mechanical
Target Quality	Default (0.050000)
Smoothing	Medium
Mesh Metric	None
Inflation	
Use Automatic Inflation	None
Inflation Option	Smooth Transition
Transition Ratio	0,272
Maximum Layers	5
Growth Rate	1,2
Inflation Algorithm	Pre
View Advanced Options	No
Advanced	
Number of CPUs for Parallel Part Meshing	Program Controlled
Straight Sided Elements	No
Rigid Body Behavior	Dimensionally Reduced
Triangle Surface Mesher	Program Controlled
Topology Checking	Yes
Pinch Tolerance	Default (9,9e-006 m)
Generate Pinch on Refresh	No
Statistics	
Nodes	71915018
Elements	50352813

TABLE 8
Model (B3) > Mesh > Mesh Controls

Object Name	*Body Sizing*	*Face Sizing 2*
State	Fully Defined	
Scope		
Scoping Method	Geometry Selection	
Geometry	1 Body	9 Faces
Definition		
Suppressed	No	
Type	Element Size	
Element Size	1,e-003 m	5,e-004 m
Advanced		
Defeature Size	Default (5,5e-006 m)	
Behavior	Soft	
Growth Rate	Default (1,2)	
Capture Curvature	No	
Capture Proximity	No	

C.1

Measured values of the wood chips

Thickness[mm]	Lenght[mm]	Width[mm]
0.3	3.8	2.8
0.5	2.5	1.9
0.2	3.7	5.6
0.4	3.1	2.6
0.6	3.8	2.0
0.4	3.5	1.5
0.6	3.6	3.1
0.3	6.7	0.7
0.4	3.2	2.3
0.2	3.2	0.9
0.4	2.9	1.9
0.5	3.6	2.2
0.4	2.9	0.7
0.2	3.8	1.1
0.4	3.0	2.4
0.6	4.2	1.6
0.7	5.0	0.7
0.5	2.8	1.0
1.1	5.1	3.5
0.3	9.5	0.6
0.5	2.8	1.5
0.5	8.3	0.9
1.0	3.1	0.8
0.4	1.8	1.2
0.3	2.9	1.5
0.5	3.7	1.5
0.6	3.3	2.5
0.2	2.2	1.0
0.4	2.1	1.6
0.8	3.2	1.5

C.2

From top to bottom: Samples in used in the measurements, larger sample size

D.1

UDFs used in case 1, 2, 3 and 4

Case 1, 2, 3 and 4: Transient wall temperature

```
/*****************************************************************************
 UDF for specifying transient boundary temperature profile
 *****************************************************************************/

#include "udf.h"

DEFINE_PROFILE(unsteady_t, thread, i)
{

    face_t f;
    real t = CURRENT_TIME;


    begin_f_loop(f,thread)
    {
    if (t <= 2220)
        {
        F_PROFILE(f, thread, i) = 293.15+ 0.216216*t;
        }
    else
        {
        F_PROFILE(f, thread, i) = 773.15;
        }
    }
    end_f_loop(f,t)
}
```

Case 1, 2: Constant energy source

```
#include "udf.h"


DEFINE_SOURCE(e_source_con,c,t,dS,eqn)
{

    real source;
    real T = C_T(c,t);
    real cp = 1062.0;
    real m_source = 0.004178413;
    real T_0 = 298.15;

    source = m_source*cp*(T-T_0);
    dS[eqn] = m_source*cp;

    return source;
}
```

Case 3 and 4 from top to bottom: Mass source, mass source CO, energy source

```c
/*****************************************************************
 UDF for specifying temperature dependent mass source

 This code will execute a constant mass source term that
 from T1[K] = 495.9 to T2 = 671.7 (222.8^oC to 398.6^oC)
 *****************************************************************/

 #include "udf.h"

DEFINE_SOURCE(m_source,c,t,dS,eqn)
 {

    real source;
    real T = C_T(c,t);


    /* Reference Tempereature [K]*/
    real T_0 = 298.15;

     if (T > 495.9 && T < 671.7)
        {
        source = 0.081;
        dS[eqn] = 0.0;
        }
    else
        {
        source = 0.0;
        dS[eqn] = 0.0;
        }
    return source;
 }
```

```c
/*****************************************************************
 UDF for specifying temperature dependent mass source

 This code will execute a constant mass source term that
 from T1[K] = 495.9 to T2 = 671.7 (222.8^oC to 398.6^oC)
 *****************************************************************/

 #include "udf.h"

DEFINE_SOURCE(m_source_co,c,t,dS,eqn)
 {

    real source;
    real T = C_T(c,t);


    /* Reference Tempereature [K]*/
    real T_0 = 298.15;

     if (T > 495.9 && T < 671.7)
        {
        source = 0.0405;
        dS[eqn] = 0.0;
        }
    else
        {
        source = 0.0;
        dS[eqn] = 0.0;
        }
    return source;
 }
```

```
/*****************************************************************
UDF for specifying energy source

This code will execute a constant energy source term
from T1[K] = 495.9 to T2[K] = 671.7 (222.8^oC to 398.6^oC)

*****************************************************************/
#include "udf.h"


DEFINE_SOURCE(e_source_func,c,t,dS,eqn)
{

   real source;
   real T = C_T(c,t);
   real cp = 1040.0;
   real T_0 = 298.15;
   real m_source = 0.081;

   if (495.9 < T && T < 671.7)
       {
       source = m_source*cp*(T-T_0);
       dS[eqn] = m_source*cp;
       }
   else
       {
       source = 0.0;
       dS[eqn] = 0.0;
       }
   return source;
}
```

D.2

Journal file (TUI-commands) used in cluster, Case 4

```
file/read-case-data cas4.cas

file/auto-save/data-frequency 150

define/user-defined/compiled-functions compile libudf yes e_source_func.c
m_source.c m_source_co.c if_trans-w-t.c "" ""

define/user-defined/compiled-functions load libudf

define/boundary-conditions/fluid cell_zone2 mixture no yes 1 no yes
"m_source::libudf" 0 0 0 1 no yes "m_source_co::libudf" 1 no yes
"e_source_func::libudf" no no no no yes no 1 no 0 yes no 1527000 no 1527000
no no 0 no 0 no 0 0 0 no 0.68 constant 1 no no 28598 no 11.6 no

define/boundary-conditions wall wall 0 no 0 no yes temperature yes yes udf
"unsteady_t::libudf" no no yes yes no 1

define/boundary-conditions wall wall:027 0 no 0 no yes temperature yes yes
udf "unsteady_t::libudf" no 1

solve/set/time-step 0.1

solve/dual-time-iterate 60000 20

file/write-data case4.dat.gz
```

D.3

Batch file used in cluster, Case 4

```
#!/bin/bash
#
# -J ns_2d_v_fsi # sensible name for the job
# -N 1         # Allocate 1 nodes for the job
# -c 20        # Idun 20 cores
#SBATCH --partition=WORKQ
#SBATCH --time=20:00:00
#SBATCH --nodes=1
#SBATCH --ntasks=20

module load FLUENT/19.2

fluent 2ddp -i compilecase4.jou -pinfiniband -t${SLURM_NTASKS} -g >stdout.out 2>error.out
```